

**Department of Physics and Astronomy**  
**Heidelberg University**

Bachelor Thesis in Physics  
submitted by

**Lucy Bovet**

born in Leipzig (Germany)

**2025**

# **Validation of the Hadronic Recoil and Electron Charge Calibration for the $W$ Boson Mass Measurement with ATLAS**

This Bachelor Thesis has been carried out by Lucy Bovet at the  
Kirchhoff Institute for Physics in Heidelberg  
under the supervision of  
apl. Prof. Dr. Monica Dunford

# Abstract

Current experimental measurements of the  $W$  boson mass are in significant tension to theoretical predictions. A precise measurement of the mass can test the Standard Model and provide insights into deviations from current theoretical models of the electroweak sector. The  $W$  boson mass cannot be measured directly but must be inferred from reconstructed decay products. Therefore, it is essential to have a detailed description of the decay kinematics. In this thesis, studies based on  $Z \rightarrow \ell^+ \ell^-$  events are presented to validate the calibration applied to Monte Carlo simulations used in the reconstruction of leptonic  $W$  boson decays. The studies are performed using data sets recorded during a dedicated low pile-up run of Run 2, corresponding to integrated luminosities of  $257 \text{ pb}^{-1}$  at 5 TeV and  $335 \text{ pb}^{-1}$  at 13 TeV.

The studies demonstrate that the simulation accurately models the boson decay with respect to various boson and lepton kinematic properties. In addition, effects from electron charge misidentification were studied. Scale factors were derived to correct discrepancies between data and simulation, ensuring a consistent modeling of the charge reconstruction. These results confirm the validity of the current simulation and provide important input for the precise determination of the  $W$  boson mass in the current ATLAS analysis.

# Zusammenfassung

Derzeitige experimentelle Messungen der  $W$ -Bosonmasse stehen in erheblichem Widerspruch zu theoretischen Vorhersagen. Eine genaue Messung der Masse kann das Standardmodell überprüfen und Einblicke in Abweichungen von aktuellen theoretischen Modellen des elektroschwachen Sektors geben. Die Masse des  $W$ -Bosons kann nicht direkt gemessen werden, sondern muss aus rekonstruierten Zerfallsprodukten abgeleitet werden. Daher ist eine detaillierte Beschreibung der Zerfallskinetik unerlässlich. In dieser Arbeit werden Studien von  $Z \rightarrow \ell^+ \ell^-$  Ereignissen vorgestellt, um die Kalibrierungsalgorithmen zu prüfen, die bei Monte-Carlo-Simulationen zur Rekonstruktion von leptonschen  $W$ -Boson-Zerfällen verwendet werden. Die Untersuchungen basieren auf Datensätzen, die während eines speziellen Low-Pile-up-Laufs von Run 2 aufgezeichnet wurden und integrierten Luminositäten von  $257 \text{ pb}^{-1}$  bei 5 TeV sowie  $335 \text{ pb}^{-1}$  bei 13 TeV entsprechen.

Die Studien zeigen, dass die Simulation den Zerfall des Bosons bezüglich verschiedenen kinematischen Eigenschaften des Bosons und der Leptonen genau modelliert. Die Auswirkungen der falschen Identifizierung der Elektronenladung wurden untersucht und Skalierungsfaktoren abgeleitet, um Diskrepanzen zwischen Daten und Simulation zu korrigieren und eine konsistente Modellierung der Ladungsrekonstruktion zu gewährleisten. Diese Ergebnisse bestätigen die Gültigkeit der Simulation und liefern einen wichtigen Beitrag zur genauen Bestimmung der  $W$ -Boson Masse in der aktuellen ATLAS-Analyse.

# Contents

<b>1</b>	<b>Introduction</b>	<b>1</b>
<b>2</b>	<b>The ATLAS Experiment at the Large Hadron Collider</b>	<b>3</b>
<b>3</b>	<b>The <math>W</math> Boson</b>	<b>6</b>
3.1	Production Asymmetry of $W^+$ and $W^-$ bosons . . . . .	6
3.2	The $W$ Boson Mass . . . . .	7
<b>4</b>	<b>Hadronic Recoil and Analysis Strategy</b>	<b>10</b>
4.1	Hadronic Recoil Definition . . . . .	10
4.2	Hadronic Recoil Calibration . . . . .	14
4.3	Mass Determination . . . . .	15
<b>5</b>	<b>Validation of the Hadronic Recoil Calibration</b>	<b>16</b>
5.1	Event Selection . . . . .	16
5.2	Calibration Checks on $Z$ Boson Quantities . . . . .	16
5.3	Calibration Checks on Lepton Quantities . . . . .	20
<b>6</b>	<b>Electron Charge Misidentification</b>	<b>24</b>
6.1	Comparison of Same-Sign and Opposite-Sign Events . . . . .	24
6.2	Single Electron Charge Identification . . . . .	26
<b>7</b>	<b>Conclusion</b>	<b>31</b>
	<b>Appendix</b>	<b>32</b>
<b>A</b>	<b>Validation of the Hadronic Recoil Calibration for the Electron Channel</b>	<b>32</b>
<b>B</b>	<b>Validation of the Hadronic Recoil Calibration with an Additional Selection Cut</b>	<b>36</b>
<b>C</b>	<b>Electron Charge Misidentification at 13 TeV</b>	<b>39</b>
	<b>List of Abbreviations</b>	<b>42</b>
	<b>Bibliography</b>	<b>44</b>

# 1 Introduction

The Standard Model (SM) of particle physics has proven to be remarkably successful in describing the fundamental forces and particles of nature. It is regarded a triumph of modern physics. Recent advances in particle physics have led to an overconstrained electroweak sector, enabling internal consistency tests of the theory. This is particularly important, as the SM is widely considered to be incomplete. So far, it does not account for phenomena such as dark matter, neutrino masses or the matter–antimatter asymmetry in the universe. One possibility for testing the validity of the SM, and for potentially finding signs of new physics, is the precision measurement of the  $W$  boson mass. This observable can be predicted from global fits to electroweak parameters within the SM framework. Comparing the theoretically derived mass with high-precision experimental measurements provides a meaningful test of the SM and may reveal deviations that indicate inadequacies in the theory [1].

The interest in independent and precise measurements of the  $W$  boson mass has significantly increased, after the CDF collaboration at Tevatron reported a measurement result with a deviation of  $7\sigma$  from the predicted SM value in 2022 [2]. Now, the ATLAS experiment at the European Organization for Nuclear Research (CERN) aims to provide a new, highly precise result for the  $W$  boson mass and thus make a key contribution to probing the SM. For this purpose, dedicated data-taking runs were conducted at the Large Hadron Collider (LHC) in 2017 and 2018, providing high-resolution data under ideal conditions for precision analyses.

A fundamental challenge in the determination of the  $W$  boson mass is the reconstruction of the neutrino kinematics in the leptonic decay of the boson. Since neutrinos escape detection and leave no direct signal in the detector, their transverse momentum must be inferred indirectly. This is achieved by estimating the hadronic recoil, which takes into account the momentum balance in the transverse plane of the event. A well-calibrated hadronic recoil is hence essential for a precise reconstruction of the  $W$  boson kinematics. The calibration is performed using  $Z$  boson events from the leptonic decay where both leptons are fully reconstructible in the final state. This provides a reliable benchmark for validating and tuning the recoil model [3].

This bachelor thesis presents dedicated calibration studies of the hadronic recoil using  $Z$  boson events. In particular, it investigates effects that have not yet been explicitly included in the current recoil calibration procedure, such as a potential dependence of the recoil on the rapidity of the  $Z$  boson. Additionally, the kinematics of the decay leptons are taken into account to verify agreement between measured data and predictions from the Monte Carlo (MC) simulation. Such validations are essential to guarantee that the recoil calibration can be reliably applied to  $W$  boson events and thus enabling a precise mass determination.

Beyond the hadronic recoil, other effects that influence the reconstruction of the  $W$  boson must also be taken into account. In a subsequent part of this thesis, the incorrect charge reconstruction of electrons <sup>1</sup> in the ATLAS detector is investigated using  $Z \rightarrow e^+e^-$  events and correction factors for the simulation are determined. A detailed investigation of these effects and their inclusion in the calibration is crucial to reduce systematic errors for the measurement of the  $W$  boson mass.

In the following, Section 2 provides an overview of the ATLAS detector at CERN, with a focus on the subdetectors relevant for particle reconstruction and charge identification. Section 3 outlines the properties of the  $W$  boson and provides the theoretical background relevant to this study. The hadronic recoil and the general analysis strategy are explained in Section 4. The recoil calibration is validated in Section 5, followed by calibration checks of the electron charge misidentification in Section 6.

---

<sup>1</sup>Charge conjugation is implied throughout this thesis.

## 2 The ATLAS Experiment at the Large Hadron Collider

The LHC is the world's largest and most powerful particle accelerator performing high-energy proton-proton (pp) and heavy-ion collisions. It is located at CERN and has been in operation since 2008. After pre-acceleration, two beams consisting of particle bunches are circulated in opposite directions through separate beam pipes, reaching energies of up to 6.8 TeV per beam. These bunches cross at four interaction points distributed around the accelerator ring, where the particle detectors ALICE, ATLAS, CMS and LHCb are located to observe the resulting collisions [4].

The analysis presented in this thesis is based on pp collision data recorded by the ATLAS detector at center-of-mass energies of  $\sqrt{s} = 5$  TeV and  $\sqrt{s} = 13$  TeV. These data were collected during dedicated low pile-up runs in 2017 and 2018, in which the number of simultaneous collisions per bunch crossing was reduced to improve the resolution of specific measurements. This data set has previously been used in the measurement of the transverse momentum spectra of  $W$  and  $Z$  bosons [5]. A detailed description of the ATLAS experiment at the LHC is given in [6] and summarized in the following.

### The ATLAS Experiment

The ATLAS detector is a general-purpose detector with forward-backward symmetry and a cylindrical geometry. It reaches approximately 25 m in height, 44 m in length and has an overall weight of about 7000 t.

The interaction point is defined as the origin of the coordinate system, with the beam line oriented along the  $z$ -axis. The transverse plane, perpendicular to the beam direction, corresponds to the  $x$ - $y$  plane and is often described using cylindrical coordinates  $(r, \phi)$ . The polar angle  $\theta$  is measured with respect to the beam axis and is used to define the pseudorapidity

$$\eta = -\log \left[ \tan \left( \frac{\theta}{2} \right) \right] . \quad (1)$$

For massive particles, the rapidity  $y = 1/2 \ln[(E + p_z)/(E - p_z)]$  is used instead.

The detector is composed of several subdetectors surrounding the collision point. These record the trajectories, momenta and energies of produced particles, enabling their identification and precise measurement [7]. A cutaway view of the ATLAS detector is shown in Figure 1.

Closest to the collision point, the Inner Detector (ID) is situated inside a thin solenoid magnet that provides a 2 T axial magnetic field. Due to the magnetic field, electrically charged particles are forced on curved trajectories. This curvature allows the measurement

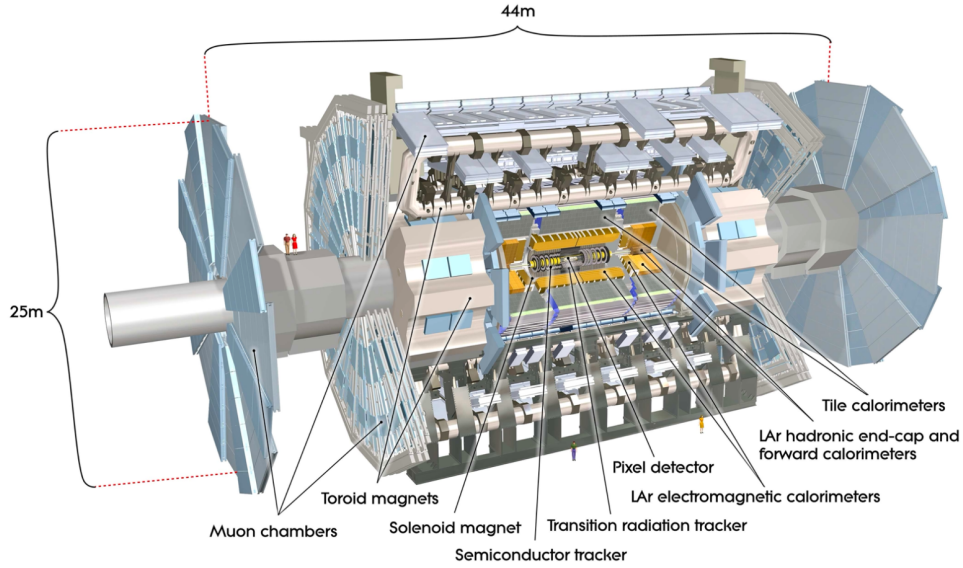


Figure 1: Schematic overview of the ATLAS detector [6].

of the particles' direction, momentum and electric charge. High-precision measurements require fine detector granularity, which is achieved by several layers of tracking detectors. The innermost components consist of pixel detectors and silicon microstrip trackers with tracking capabilities up to  $|\eta| < 2.5$ . These are followed by the gas-filled straw tubes of the Transition Radiation Tracker (TRT), covering the pseudorapidity range  $|\eta| < 2$ . The TRT contributes significantly to the momentum measurement due to the large number of tracking points and the long track length. In particular, it provides good electron identification by detecting transition radiation photons emitted in the gas mixture of the straw tubes, which helps distinguish electrons from hadrons.

At higher absolute pseudorapidity values  $|\eta|$ , the number of detector hits per track decreases, reducing the precision of trajectory reconstruction. This effect results from the geometry of the ID, where particles at shallow angles cross fewer active layers of the sub-detectors. A quarter section of the ID together with the electromagnetic calorimeter is illustrated in Figure 2 with various values of  $|\eta|$  highlighted.

The subsequent liquid-argon (LAr) electromagnetic sampling calorimeters provide high-resolution energy and position measurements in the barrel region  $|\eta| < 1.475$  and extend into the end-cap regions  $1.375 < |\eta| < 3.2$ . Within the pseudorapidity range matched to the ID coverage, the calorimeter has a particularly fine granularity. In this region, it is segmented into three layers in depth, making it especially well suited for precision measurements of electrons and photons. However, in the transition region between the barrel and end-cap calorimeters  $1.375 < |\eta| < 1.52$ , the electromagnetic calorimeter performance is reduced, as illustrated in Figure 2.

The following hadronic sampling calorimetry system consists of a scintillating tile calorime-



ter in the central region  $|\eta| < 1.7$  using steel as the absorber and LAr end-cap calorimeter for ranges  $1.5 < |\eta| < 3.2$ . At especially high absolute pseudorapidity regions,  $3.1 < |\eta| < 4.9$ , the forward calorimeter consisting of three layers collects energy depositions close to the beam line.

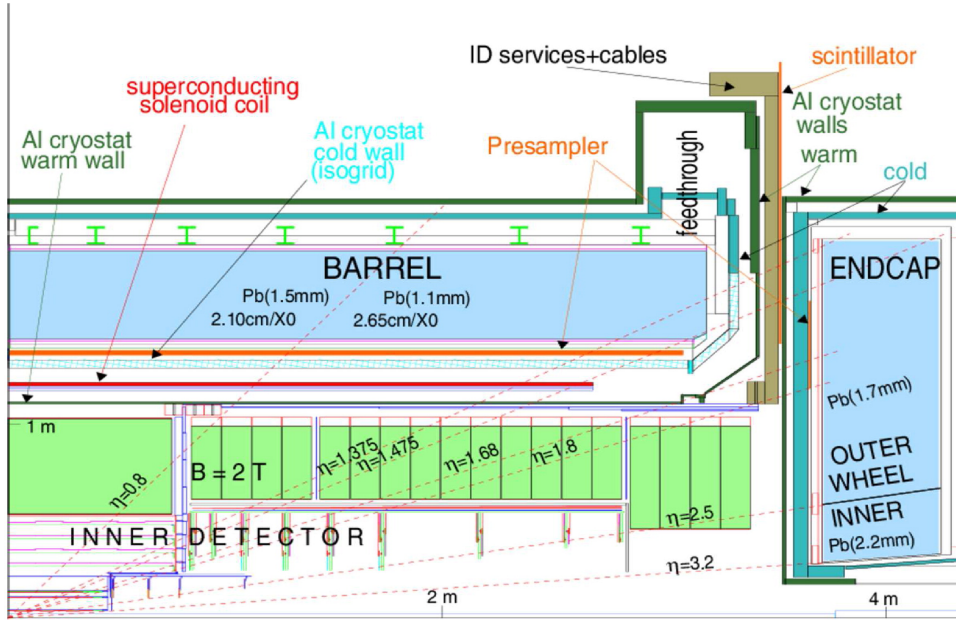


Figure 2: Longitudinal cutaway view of one quarter of the ATLAS detector cross section up to the electromagnetic calorimeter, as recorded during Run 1 [8].

Lastly, the muon spectrometer precisely determines the momentum of muons by measuring their deflection in a magnetic field generated by large superconducting air-core toroid magnets. Muon tracks are bent by the barrel toroid in the region up to  $|\eta| < 1.4$  and by the end-cap toroids in the range  $1.6 < |\eta| < 2.7$ . In the transition region between, both magnetic field systems contribute to the deflection. The muon system is instrumented with separate trigger and high-precision tracking chambers. In the barrel region, the chambers are arranged in three cylindrical layers around the beam axis to measure the muon tracks, whereas in the transition and end cap area, the chambers are installed as planes in three layers perpendicular to the beam axis. The track coordinates are measured across most of the pseudorapidity range using Monitored Drift Tubes. In the forward region  $2 < |\eta| < 2.7$  Cathode Strip Chambers are used instead.

The pp interaction rate at the collision point can reach up to 40 MHz, however the event data recording rate is limited to 1 kHz. The event rejection is achieved by a trigger system consisting of a Level-1 trigger reducing data to 100 kHz only using a subset of detector information, followed by the High Level Trigger reaching a reduction to the desired 1 kHz [9].

### 3 The $W$ Boson

The known elementary particles and their interactions are described with remarkable precision in the SM. However, it is considered to be incomplete, as it cannot explain fundamental observations such as the matter-antimatter asymmetry in the universe or the existence of dark matter yet. Therefore, precise measurements of fundamental parameters of the SM are essential for testing and eventually expanding the model [2].

The research conducted at CERN, including experiments at the ATLAS detector, addresses these open questions in fundamental physics. Among the many research topics at ATLAS, the properties of the  $W$  boson play a key role in testing the internal consistency of the SM and in the search for potential signs of new physics.

A comprehensive introduction to the fundamental principles of particle physics can be found in [10], which serves as the main source for the following summary of key concepts relevant to this thesis.

#### 3.1 Production Asymmetry of $W^+$ and $W^-$ bosons

According to the SM, the electroweak interaction is mediated by the  $W$  and  $Z$  boson as well as the photon, where the  $W$  boson is a massive particle that can either carry a positive charge,  $W^+$ , or a negative charge  $W^-$ . The analysis is based on studying the decay of the  $W$  boson into a charged lepton  $\ell^\pm$  and a neutrino  $\nu$ , i.e.  $W^\pm \rightarrow \ell^\pm \nu$ , as illustrated in Figure 3. The reconstructed charge of the lepton identifies whether the decaying boson was a  $W^+$  or a  $W^-$  as a consequence of charge conservation.



Figure 3: Production of a  $W^\pm$  boson through quark-antiquark annihilation and subsequent decay into a lepton-neutrino pair.

However, at the LHC,  $W^+$  bosons are produced more frequently than  $W^-$  bosons. This asymmetry arises from the internal structure of the colliding protons.

Besides three valence quarks,  $(u, u, d)$ , the proton contains a sea of virtual gluons  $g$  which can produce quark-antiquark pairs through pair production  $g \rightarrow q\bar{q}$ . The dynamic interactions between all quarks and gluons lead to a probabilistic distribution of their momenta within the proton. These momentum distributions are described by the Parton Distribution Functions (PDFs).

The PDF of the up quark,  $u(x)$ , can be decomposed into contributions from valence quarks,  $u_V(x)$ , and sea quarks,  $u_S(x)$ . The same applies for the down quark PDF

$$u(x) = u_V(x) + u_S(x) \quad \text{and} \quad d(x) = d_V(x) + d_S(x) . \quad (2)$$

Because a proton contains two valence up quarks and one valence down quark, the valence PDFs are normalized accordingly

$$\int_0^1 u_V(x) dx = 2 \quad \text{and} \quad \int_0^1 d_V(x) dx = 1 . \quad (3)$$

In contrast, the PDFs for the antiup and antidown quarks receive contributions only from sea quarks and are therefore given by

$$\bar{u}(x) = \bar{u}_S(x) \quad \text{and} \quad \bar{d}(x) = \bar{d}_S(x) . \quad (4)$$

Furthermore, two assumptions can be made for the sea quark PDFs. First, since sea quark and sea antiquark are produced in pairs, their PDFs are equal within the same flavor. Second, due to the small mass difference between up and down quarks, the sea quark PDFs of both flavors can be assumed to be approximately equal. These assumptions lead to

$$u_S(x) = \bar{u}_S(x) \approx d_S(x) = \bar{d}_S(x) . \quad (5)$$

While  $W^+$  bosons are produced by up and antidown quarks ( $u, \bar{d}$ ),  $W^-$  bosons result from interactions between down and antiup quarks ( $d, \bar{u}$ ). As a consequence, the unequal PDFs for up and down quark lead to a production asymmetry of  $W^+$  and  $W^-$  bosons in pp collisions at the LHC.

### 3.2 The $W$ Boson Mass

The gauge theory describing the electroweak interactions incorporates the masses of the  $W$  and  $Z$  bosons,  $m_W$  and  $m_Z$ , and implies the existence of the Higgs boson. In 1983 the  $W$  and  $Z$  bosons were discovered at CERN SPS [11, 12] and in 2012 the LHC collaborations ATLAS and CMS reported the existence of the Higgs boson and its mass [13, 14]. Since the observation of the Higgs boson, the electroweak sector of the SM is fully constrained by experimental measurements. The  $Z$  boson mass has been measured with remarkable precision to  $m_Z = 91\,188.0 \pm 2.0$  MeV by experiments at the CERN LEP collider. In contrast, the uncertainty in the  $m_W$  measurement at LEP was an order of magnitude larger than that of  $m_Z$ . This is mainly due to the lower production rate of  $W$  boson pairs in electron-positron collisions, which is several orders of magnitude smaller than that of  $Z$  bosons [2].

At lowest order the  $W$  boson mass  $m_W$  can be expressed in terms of the  $Z$  boson mass  $m_Z$ , the fine-structure constant  $\alpha$  and the Fermi constant  $G_\mu$ . Higher order corrections  $\Delta r$  are sensitive to the gauge couplings and masses of heavy particles within the SM, particularly the top quark and the Higgs boson. In relation to these parameters the  $W$  boson mass can be expressed with

$$m_W^2 \left( 1 - \frac{m_W^2}{m_Z^2} \right) = \frac{\pi\alpha}{\sqrt{2}G_\mu} (1 + \Delta r) . \quad (6)$$

This equation demonstrates that the SM is overconstrained. The  $W$  boson mass can either be measured directly or determined indirectly through measurements of  $m_Z$ ,  $\alpha$ ,  $G_\mu$  and  $\Delta r$ . Thus, a precise  $m_W$  measurement tests the SM's internal consistency [1]. Extended theories that can modify  $\Delta r$  include contributions from additional particles and interactions, such as potential new heavy particles that cannot be probed directly by accelerators yet [2]. A significant discrepancy between measured and predicted values can therefore be an indicator for Physics beyond the Standard model (BSM). Currently the precision of the  $W$  boson mass measurement sets limitations on constraints for BSM scenarios [1].

The  $W$  boson mass determined from electroweak parameters, the so-called global electroweak fit, yields a precise value of  $m_W = 80\,353 \pm 6$  MeV [15]. However, current experimental results show a certain tension. On the one hand four independent measurements performed by the LEP, Tevatron and LHC experiments gained the average experimental value of  $m_W = 80\,369.2 \pm 13.3$  MeV. In contrast, a single measurement by the CDF Collaboration at the Fermilab Tevatron reported a value of  $m_W = 80\,433.5 \pm 9.4$  MeV, which stands in strong disagreement with previous measurements and deviates by  $7\sigma$  from the global electroweak fit prediction, thereby challenging the SM. Most recently, in 2024 the CMS experiment published a new measurement result of  $m_W = 80\,360.2 \pm 9.9$  MeV, which is consistent with SM predictions. All current experimental results of  $W$  boson mass measurements can be compared in Figure 4, including the latest result from CMS [2].

The CMS result from 2024 is remarkable due to its precision of 0.12 permil. Their research was based on a data set with more than twice the pile-up than any other  $m_W$  measurement before and only reconstructed events from the muon channel of the leptonic decay were used [2]. The current ATLAS research aims to achieve a similar level of precision, working with low pile-up data and including both the muon and electron channel in the analysis.

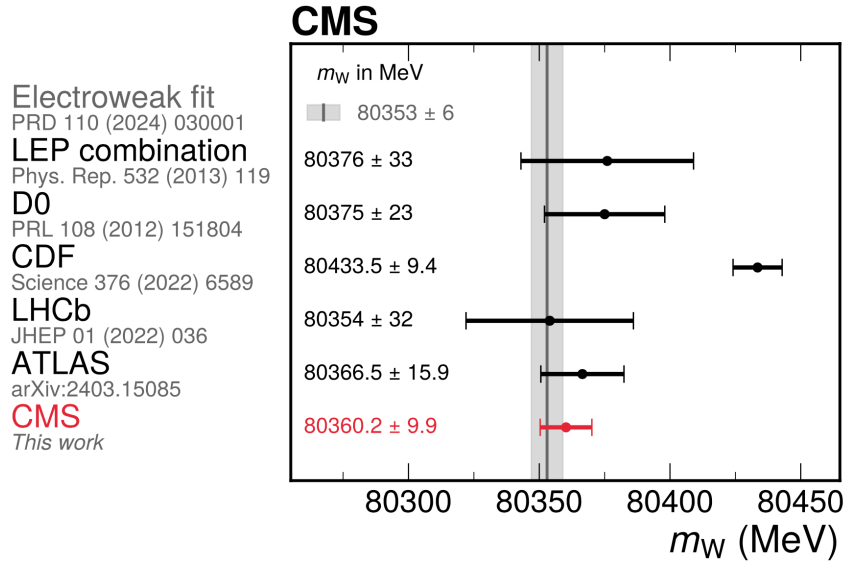


Figure 4: Comparison between measurement results by the LEP, Tevatron and LHC experiments and the electroweak fit prediction, which is represented by the gray vertical band showing its uncertainty [2].

## 4 Hadronic Recoil and Analysis Strategy

In the leptonic decay, the  $W$  boson cannot be fully reconstructed, since neutrinos are not directly detectable in collider experiments. Nevertheless, the kinematic properties of the charged lepton and the neutrino are essential for determining  $m_W$ . The standard approach to reconstruct the neutrino kinematics in high-precision ATLAS analyses involving  $W$  bosons relies on the so-called *hadronic recoil*. Its reconstruction and calibration leading to the determination of  $m_W$  are described below, following the approach outlined in [3].

### 4.1 Hadronic Recoil Definition

The hadronic recoil is defined as the vectorial sum of all transverse momenta of particles from initial-state radiation (ISR) of gluons and quarks. Since the initial pp collision occurs along the beamline and has no net transverse momentum, the hadronic recoil directly reflects the transverse momentum of the  $W$  boson. Additionally, the transverse momentum of the neutrino can be inferred from momentum conservation. The quantities are related as

$$\vec{p}_T^V = \vec{p}_T^\ell + \vec{p}_T^\nu = - \sum_{i=ISRq,g} \vec{p}_{T,i} = -\vec{u}_T . \quad (7)$$

Here,  $\vec{p}_T^V$  denotes the transverse momentum of the  $W$  boson, while  $\vec{p}_T^\ell$  and  $\vec{p}_T^\nu$  represent the transverse momenta of the charged lepton  $\ell$  and the neutrino  $\nu$ , respectively. The hadronic recoil is denoted by  $\vec{u}_T$ .

The calculation of the hadronic recoil is performed by the *Particle Flow* algorithm, which selects reconstructed particles, the *Particle Flow Objects* (PFOs), detected in the ID and Calorimeters of the ATLAS detector. In the transverse plane, the hadronic recoil is then obtained as the vectorial sum of all electrically charged and neutral PFOs. For a more detailed description, see [3, Section 2].

The corresponding data for this analysis were collected under low pile-up conditions with an average number of interaction per crossing of  $\langle\mu\rangle \approx 2$ , facilitating particle identification [5]. With  $\vec{u}_T$  given, the neutrino transverse momentum  $\vec{p}_T^\nu$  can be determined via

$$\vec{p}_T^\nu = -(\vec{u}_T + \vec{p}_T^\ell) . \quad (8)$$

Together with the azimuthal angle  $\phi^\nu$  of  $\vec{p}_T^\nu$ , the transverse mass of the  $W$  boson can then be calculated as

$$m_T = \sqrt{2\vec{p}_T^\ell \vec{p}_T^\nu (1 - \cos(\phi^\ell - \phi^\nu))} . \quad (9)$$

Another important property to quantify are contributions from the underlying event, pile-up and emissions beyond first hard emission. These effects can be characterized by first considering the total transverse event activity,  $\sum E_T$ , defined as the scalar sum of the transverse momenta  $\vec{p}_T$  of all PFOs. This quantity is directly correlated with the resolution of the hadronic recoil measurement and strongly depends on the vector boson kinematics. The value of  $\sum E_T$  increases for higher values of  $p_T^V$  and consequently  $u_T$ . A description of the underlying event, is now achieved by defining a recoil-corrected event activity,  $\sum \bar{E}_T = \sum E_T - u_T$ , effectively subtracting recoil contributions from the total transverse event activity.

The kinematic relations above are also applicable to  $Z \rightarrow \ell^+ \ell^-$  decays where the undetected  $\vec{p}_T^\nu$  is replaced by the transverse momentum of the second lepton  $\vec{p}_T^\ell$ . In these events the kinematics of the two leptons can be reconstructed with a resolution that is approximately one order of magnitude better than that of the hadronic recoil measurement.

### Hadronic Recoil in $Z$ Events

In the analysis,  $Z$  boson events are used to calibrate the hadronic recoil comparing measured data with predictions from the MC simulation. In this decay, the recoil can be compared to the directly measured transverse momenta of the two decay leptons, which corresponds to the transverse momentum of the  $Z$  boson  $\vec{p}_T^{\ell\ell} = \vec{p}_T^Z$ . The comparison between  $\vec{u}_T$  and  $\vec{p}_T^{\ell\ell}$  probes the detector's response to hadronic activities. In Figure 5 a  $Z$  boson event is illustrated in the transverse plane. The direction of  $\vec{p}_T^{\ell\ell}$  is used as reference to define scalar quantities from projections of  $\vec{u}_T$ .

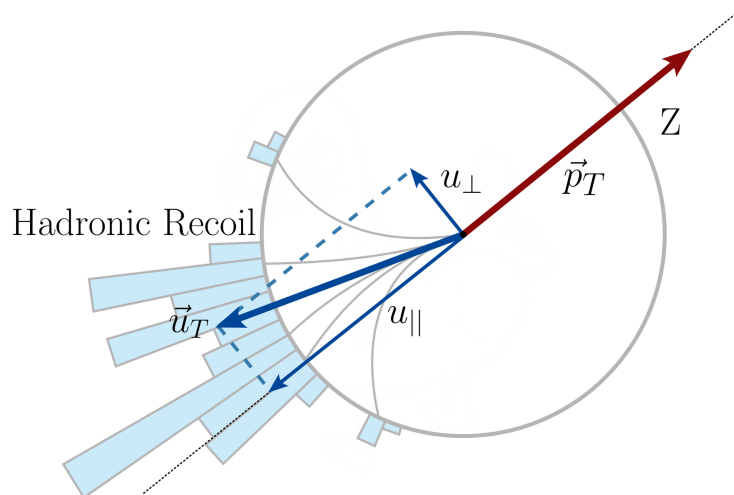


Figure 5: Production of a  $Z$  boson in the transverse plane and visualization of the hadronic recoil components perpendicular and parallel to the boson axis [16].

- The perpendicular component of the hadronic recoil is given by

$$u_{\perp} = \frac{|\vec{p}_T^{\ell\ell} \times \vec{u}_T|}{p_T^{\ell\ell}}. \quad (10)$$

This quantity is Gaussian-like distributed around zero,  $\langle u_{\perp} \rangle = 0$ , since measurement inaccuracies are randomly distributed around  $\vec{p}_T^{\ell\ell}$ . The distribution's width  $\sigma(u_{\perp})$  reflects the resolution of the hadronic recoil perpendicular to  $\vec{p}_T^{\ell\ell}$ .

- The parallel component of the hadronic recoil is given by

$$u_{\parallel} = \frac{\vec{p}_T^{\ell\ell} \cdot \vec{u}_T}{p_T^{\ell\ell}}. \quad (11)$$

Ideally  $u_{\parallel} \approx -p_T^{\ell\ell}$  should apply, which would be valid in case of a perfect detector response and no scalar error while estimating  $u_{\parallel}$ . In order to test this estimation the bias is defined.

- The Bias is suitable to test the over- or underestimation of  $u_{\parallel}$  by its definition

$$b = u_{\parallel} + p_T^{\ell\ell}. \quad (12)$$

In case of  $u_{\parallel} = -p_T^{\ell\ell}$  the bias is zero. However, usually it is Gaussian-like distributed around  $\langle b \rangle > 0$  due to insufficient particle detection which leads to an underestimation of  $u_{\parallel}$ . The width of this distribution,  $\sigma(b)$ , reflects the hadronic recoil resolution parallel to  $\vec{p}_T^{\ell\ell}$ .

As an example, the distribution of those three quantities in the muon decay channel for  $Z$  boson events at 5 TeV can be seen in Figure 6.

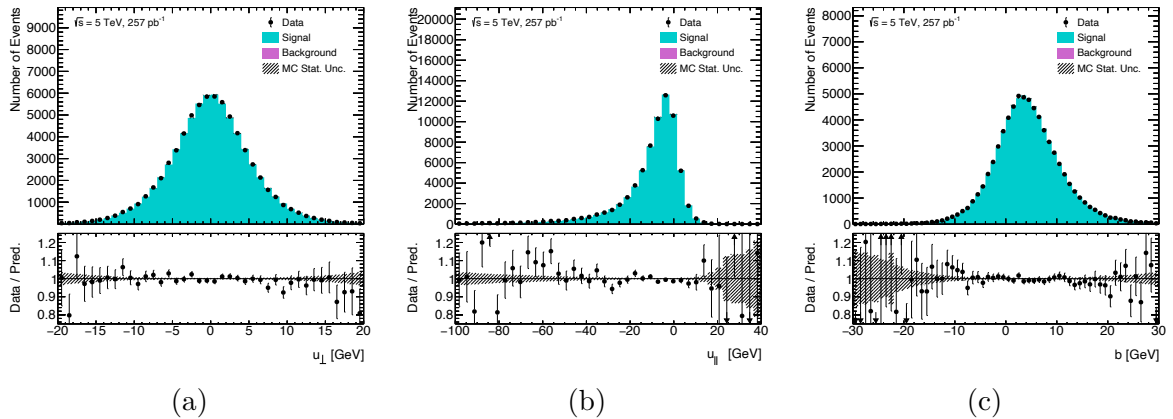


Figure 6: Distributions of (a) the perpendicular recoil component  $u_{\perp}$ , (b) the parallel recoil component  $u_{\parallel}$  and (c) the bias  $b$  in the  $Z \rightarrow \mu^+\mu^-$  decay channel at 5 TeV with a data-to-MC comparison. These distributions are shown after calibration, where data and MC predictions align well.



## Hadronic Recoil in $W$ Events

In Figure 7 the decay of a  $W$  boson in the transverse plane is illustrated. In those events the boson axis cannot be determined by data due to the missing neutrino  $\vec{p}_T^\nu$ . Therefore, the hadronic recoil is projected on the charged lepton axis by defining:

$$u_\perp^\ell = \frac{|\vec{p}_T^\ell \times \vec{u}_T|}{p_T^\ell}, \quad (13)$$

and

$$u_\parallel^\ell = \frac{\vec{p}_T^\ell \cdot \vec{u}_T}{p_T^\ell}. \quad (14)$$

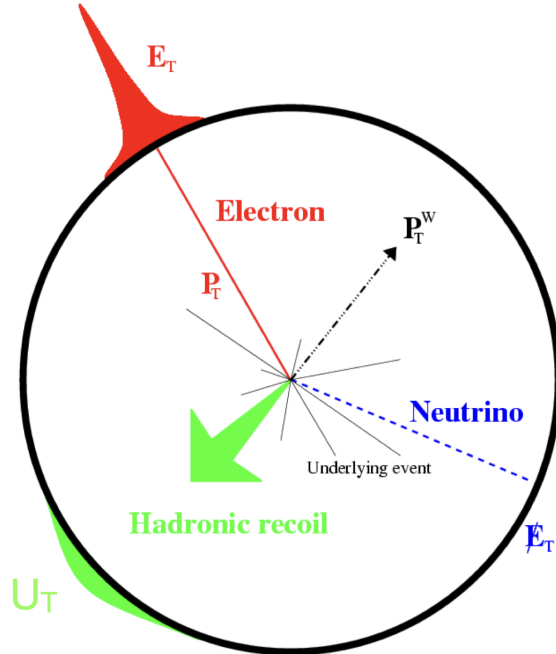


Figure 7: Visualization of the decay components of a  $W$  boson into an electron and a neutrino in the transverse plane. The hadronic recoil is shown in green, resulting in a Gaussian-like detector response profile. Similarly, the detector response for the electron is illustrated in red. The neutrino, depicted in blue, can be indirectly inferred from the missing transverse energy. The underlying event is approximately symmetrically distributed in the transverse plane as indicated in grey [17].

For both  $Z$  and  $W$  events, these scalar quantities describe the two-vector  $\vec{u}_T$  based on the boson kinematics. This is more useful than relying on the  $x$ - and  $y$ -axes.

## 4.2 Hadronic Recoil Calibration

The calibration of the hadronic recoil is performed using  $Z$  boson events, where correction factors are derived and subsequently applied to  $W$  boson events. The following calibration steps are performed consecutively and corrections are retrieved separately for data at 5 TeV and 13 TeV. A detailed description of the calibration procedure is given in [3, Section 6]. This section summarizes the key steps.

Overall a calibration transfer from  $Z$  boson to  $W$  boson events can be applied with high accuracy since both events show similar behavior. However, slight differences occur in the energy scale and the PDFs, affecting the underlying event activity  $\sum \bar{E}_T$  and the transverse momentum spectra of the vector boson  $p_T^V$ . Therefore, the calibration must be a function of  $\sum \bar{E}_T$  and  $p_T^V$ , to transfer the corrections from  $Z$  to  $W$  events. The steps performed to correctly model the correlation between  $\sum \bar{E}_T$  and  $p_T^V$  in MC are:

- A 2D reweighting is obtained from the ratio of normalized 2D distributions as functions of  $(\sum \bar{E}_T, p_T^{\ell\ell})$  comparing data to MC for  $Z$  events in the electron and muon channel. For the application to the  $W$  boson simulation  $p_T^{\ell\ell}$  is replaced by  $p_T^{true,W}$  using the reweighting coefficients determined from  $Z$  boson events.
- Whereas the first reweighting applies well to  $Z$  events, for  $W$  events it is insufficient and a correction procedure based on data from  $W$  boson decays is needed. An improved modeling of  $\sum \bar{E}_T$  for  $W$  events is achieved by a reweighting of  $\sum \bar{E}_T$  in bins of  $u_T$ .
- The application of both reweightings modifies the spectrum of  $p_T^{true,V}$ , but for  $W$  events a modeling of this quantity is crucial. Thus, to recover the initial spectrum, an additional reweighting in  $p_T^{true,V}$  is applied.

In addition to a correct modelling of  $\sum \bar{E}_T$  and  $p_T^V$ , the modeling of the azimuthal direction of the recoil in the simulation needs to be corrected. This is done empirically by an additive offset. For  $x$  and  $y$  components each, the differences of the mean values of the recoil from data in  $Z$  boson events and in the simulation is taken. These offsets are fitted with a first-order polynomial depending on  $\sum \bar{E}_T$ .

Furthermore, the resolution and response of the recoil components  $u_{\parallel}$  and  $u_{\perp}$  in the MC simulation are reweighted to match those observed in data, resulting in a corrected recoil observable.

### 4.3 Mass Determination

With the hadronic recoil calibrated and the kinematic distributions of the lepton and neutrino reconstructed, an optimal estimate of  $m_W$  is obtained through a global profile likelihood fit. This fit evaluates the compatibility between the data and the calibrated MC predictions. It is performed using the distributions of the lepton transverse momentum  $p_T^\ell$  and the transverse mass of the  $W$  boson,  $m_T$ . In Figure 8 simulated distributions are illustrated for different variations of the values for the  $W$  boson mass  $m_W$  and its distribution width  $\Gamma_W$ . By varying these values in relation to a reference value the expected signal and background distribution change. Therefore, several simulations can be compared to the measured data in the kinematic distributions in order to find an optimal agreement for a value of  $m_W$  [18].

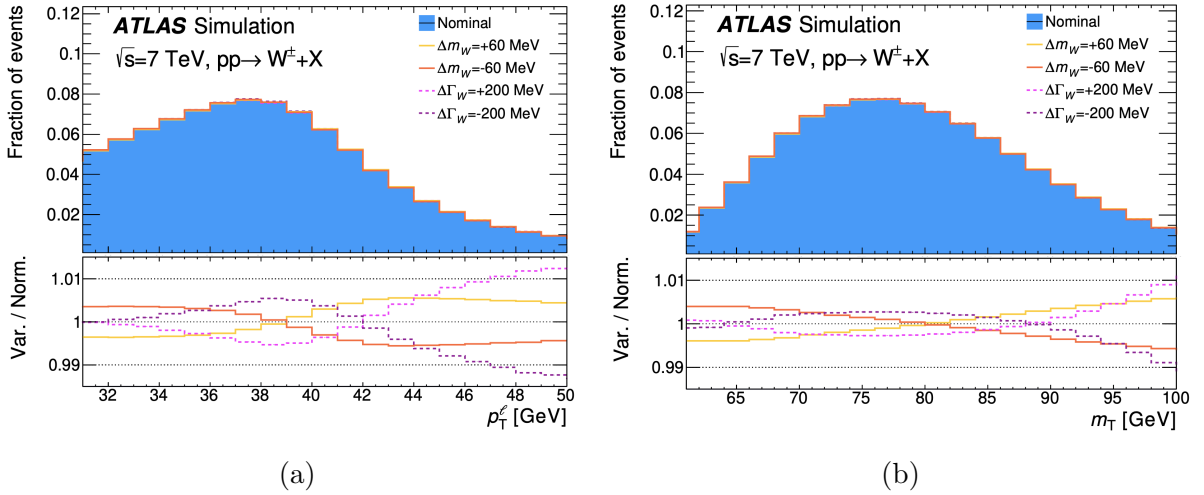


Figure 8: Simulations of the kinematic distributions of (a) the lepton transverse momentum  $p_T^\ell$  and (b) the transverse mass  $m_T$ , for  $W$  boson mass and width values of  $m_W = 80399$  MeV and  $\Gamma_W = 2085$  MeV. The lower ratio panels illustrate the effects of varying these parameters by  $\pm 60$  MeV and  $\pm 200$  MeV, respectively [18].

## 5 Validation of the Hadronic Recoil Calibration

An accurate calibration of the MC simulation to data from  $Z$  boson decays is essential for a reliable application to subsequent  $W$  boson analyses. In particular, the scale and resolution of the hadronic recoil components, both parallel and perpendicular to the boson axis, must show good agreement between simulation and data. Therefore, calibration checks are performed for the perpendicular component of the hadronic recoil,  $u_{\perp}$ , and the parallel component, represented by the bias  $b$ . Additionally, the modeling of the underlying event activity  $\sum \bar{E}_T$  is tested.

This chapter provides an overview of the calibration tests performed between MC simulation and data for the  $Z \rightarrow \mu^+\mu^-$  decay at 5 TeV with an integrated luminosity of  $257 \text{ pb}^{-1}$ . Further validations for the  $Z \rightarrow e^+e^-$  decay at 5 TeV are presented in Appendix A. The results of all comparisons show excellent agreement between data and simulation.

### 5.1 Event Selection

The final  $Z$  boson events used for the calibration are selected with various criteria to optimize the data base. A detailed description is provided in [3, Section 4]. Considered events are required to have at least one primary vertex with a minimum of two tracks. The subsequent identification of muons and electrons is achieved by demanding isolation from other tracks in the ID, respectively using the *Medium* or *MediumLH* working point. Additionally, both reconstructed leptons must be exactly two of the same flavor, but with opposite charge and a transverse momentum of  $p_T^{\ell} > 25 \text{ GeV}$ . This dilepton system must satisfy an invariant mass of  $66 < m_{\ell\ell} < 116 \text{ GeV}$ . Besides, the effect of an another event selection was studied requiring furthermore  $u_T < 25 \text{ GeV}$ .

### 5.2 Calibration Checks on $Z$ Boson Quantities

First, a validation of the recoil calibration is performed on variables describing the properties of the decaying  $Z$  boson. Since the  $Z$  boson is a massive particle, the rapidity  $y$  must be used when describing the decay direction relative to the beam axis.

#### Rapidity of the $Z$ Boson

The hadronic recoil calibration procedure, described in Subsection 4.2, applies corrections to achieve better agreement between data and simulation. However, no reweighting is applied with respect to the rapidity  $y$  of the  $Z$  boson. The control plots in Figure 9 demonstrate that the recoil components are not dependent on the  $Z$  boson rapidity and that data and MC simulation are in good agreement. As an example, a data-to-MC comparison for the mean value  $\langle u_{\perp} \rangle$  and the resolution  $\sigma(u_{\perp})$  is presented here.

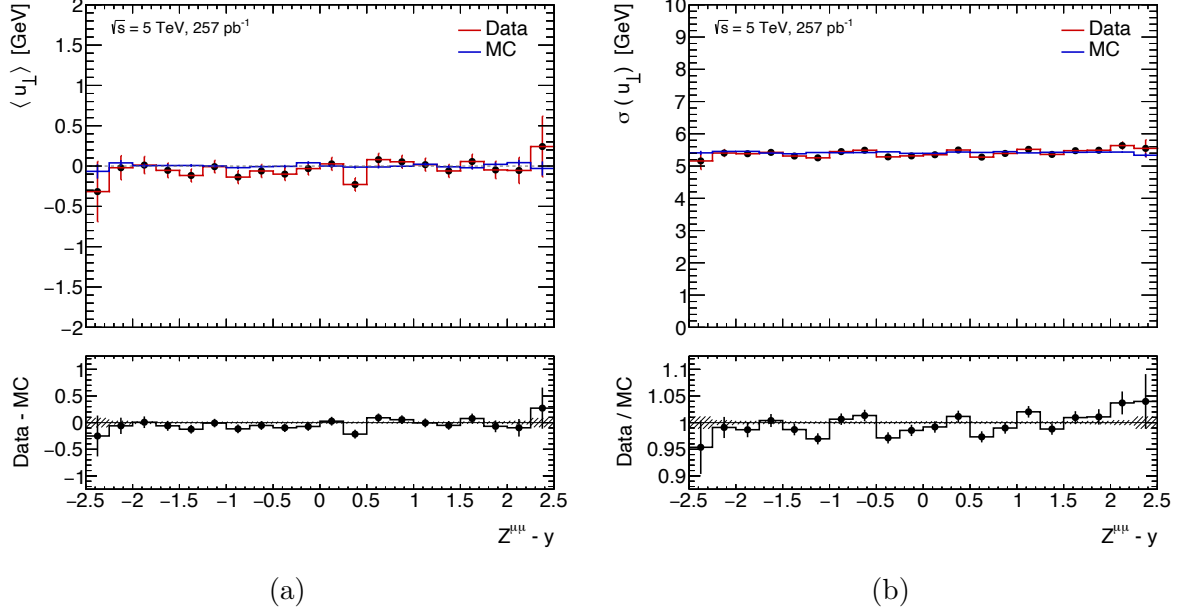


Figure 9: Data-to-MC comparison of (a) mean value  $\langle u_{\perp} \rangle$  and (b) resolution  $\sigma(u_{\perp})$  of the perpendicular hadronic recoil component as a function of the  $Z$  boson rapidity  $y$ .

Similar calibration checks of the underlying event activity,  $\sum \bar{E}_T$ , are shown in Figure 10. Good agreement between data and MC is observed and variations in the  $Z$  boson rapidity  $y$  have no significant impact on the underlying event.

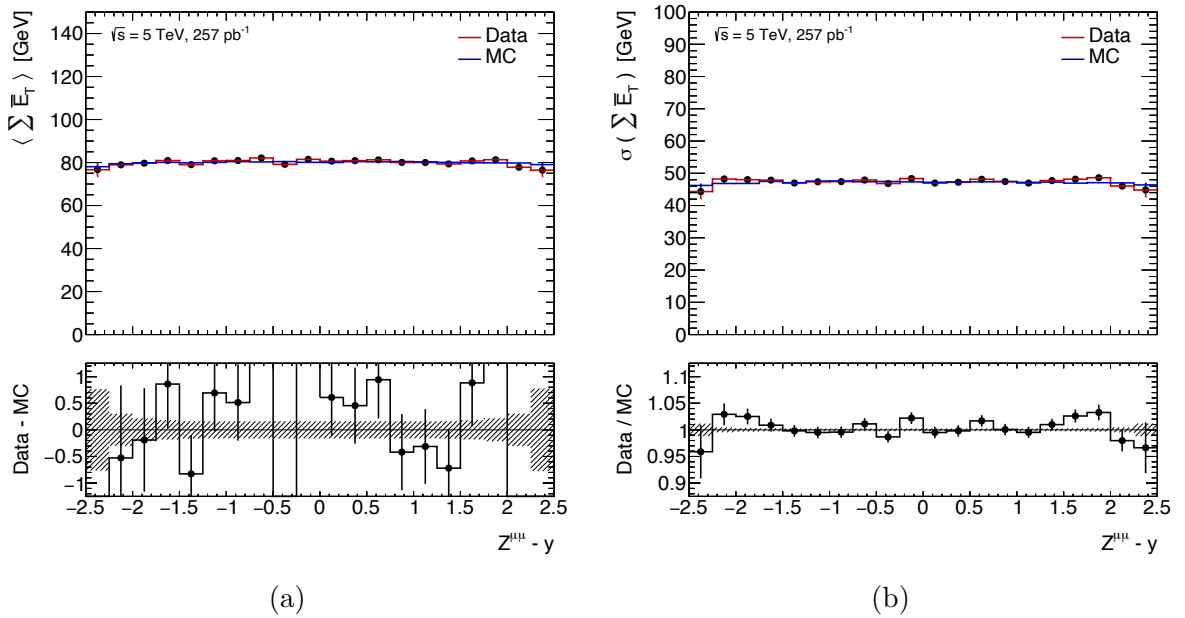


Figure 10: Data-to-MC comparison of (a) mean value  $\langle \sum \bar{E}_T \rangle$  and (b) resolution  $\sigma(\sum \bar{E}_T)$  of the underlying event activity as a function of the  $Z$  boson rapidity  $y$ .

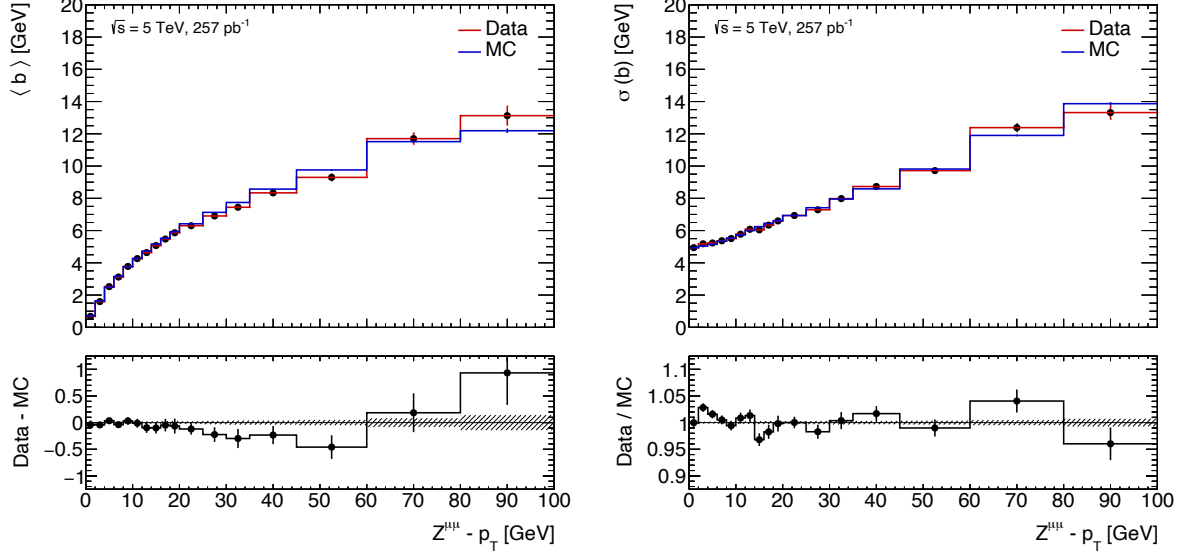
## Transverse Momentum of the $Z$ Boson

Besides the rapidity, the transverse momentum of the  $Z$  boson,  $p_T^Z$ , is a sensitive observable to validate the calibration. As illustrated in Figure 11 the bias  $b$  shows a clear dependence on  $p_T^Z$  that is well calibrated in the MC simulation and in good agreement with the data.

It can be seen in Figure 11a that  $\langle b \rangle$  increases with  $p_T^Z$ . This is due to the fact that  $b$  is by definition directly related to  $p_T^Z$  via  $b = u_{\parallel} + p_T^Z$ . Moreover, a higher transverse momentum of the  $Z$  boson corresponds to increased ISR from quarks and gluons, as shown in Equation 7. Stronger ISR in turn leads to more complex event topologies and greater hadronic activity, which challenges the detector's reconstruction performance. As a result, the parallel recoil component  $u_{\parallel}$  tends to be underestimated with respect to  $p_T^Z$ , hence explaining  $\langle b \rangle$  increasing with  $p_T^Z$ . This trend is also reflected in the increasing  $\sigma(b)$  as a function of  $p_T^Z$ , indicating reduced precision in the estimation of  $u_{\parallel}$  at higher transverse momenta. Nevertheless, the relative resolution  $\sigma(b)/p_T^Z$  improves with increasing  $p_T^Z$ , since  $p_T^Z$  rises more rapidly than the corresponding resolution.

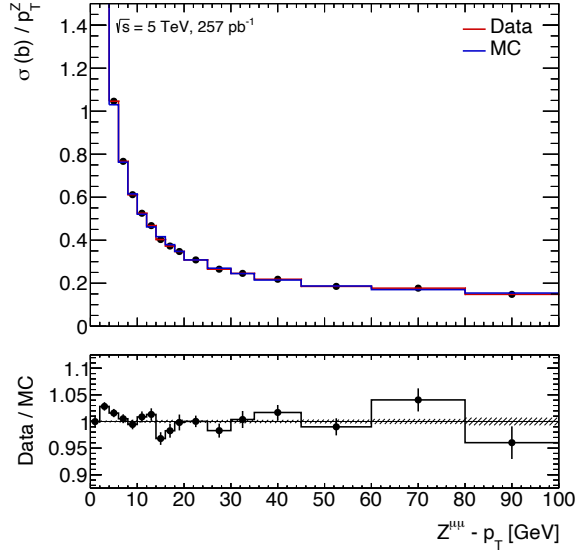
Additionally, an increase of the underlying event activity  $\sum \bar{E}_T$  with rising  $p_T^Z$  is presented in Figure 12. This can be explained by looking at the components of  $\sum \bar{E}_T$ . While  $\sum E_T$  is defined as the scalar sum of the transverse momenta of all PFOs,  $u_T$  denotes the absolute value of the vector sum of transverse momenta from ISR. When deriving the underlying event activity via  $\sum \bar{E}_T = \sum E_T - u_T$ , transverse momentum components of ISR that are perpendicular to  $p_T^Z$  remain in  $\sum \bar{E}_T$ , since they are not subtracted by the vector sum  $u_T$ . As a result,  $\sum \bar{E}_T$  increases with  $p_T^Z$ , reflecting the enhanced ISR and broader hadronic activity at higher boson transverse momentum.

The calibration checks presented here demonstrate a good agreement of recoil components and underlying event activity as functions of either the rapidity  $y$  or the transverse momentum  $p_T^Z$  of the  $Z$  boson, each integrated over the full range of the respectively other variable. In addition, further two-dimensional calibration checks in  $y$  and  $p_T^Z$  have been performed, confirming the consistency of the simulation with the data across both variables simultaneously.



(a)

(b)



(c)

Figure 11: Data-to-MC comparison of (a) mean value  $\langle b \rangle$ , (b) absolute resolution  $\sigma(b)$  and (c) relative resolution  $\sigma(b)/p_T^Z$  of the bias as a function of the  $Z$  boson transverse momentum  $p_T^Z$ .

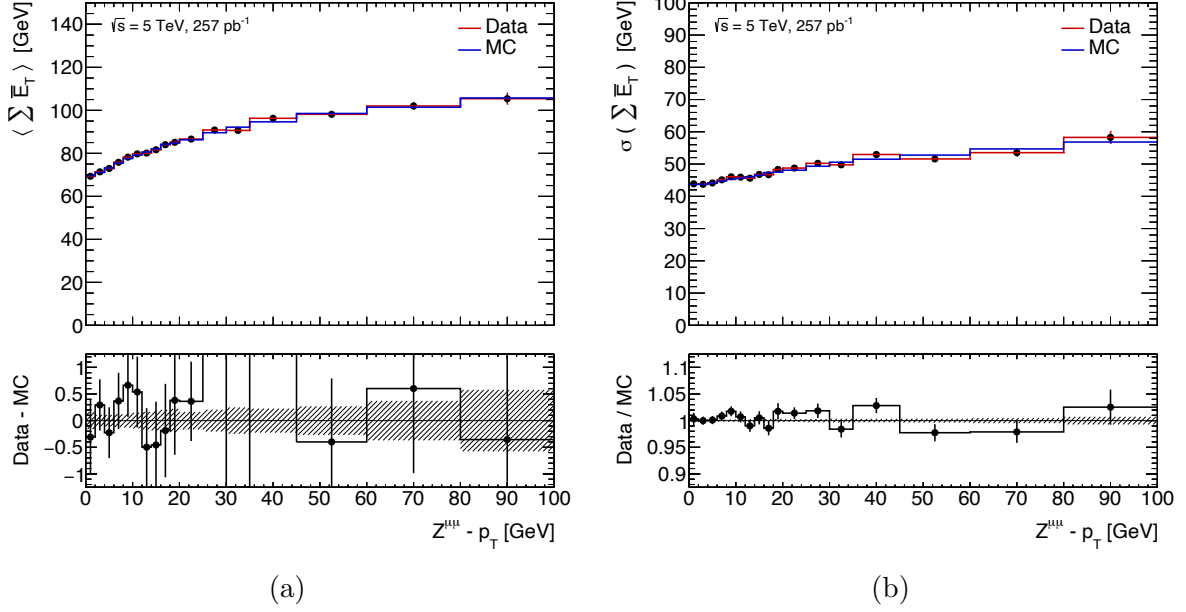


Figure 12: Data-to-MC comparison of (a) mean value  $\langle \sum \bar{E}_T \rangle$  and (b) resolution  $\sigma(\sum \bar{E}_T)$  of the underlying event activity as a function of the  $Z$  boson transverse momentum  $p_T^Z$ .

### 5.3 Calibration Checks on Lepton Quantities

The  $Z$  boson decays into two oppositely charged leptons. The correlation between the kinematic distributions of the leptons and the hadronic recoil components can be studied to validate the MC simulation further and, if necessary, refine its calibration. Since the reconstruction of the kinematic properties of the leptons is independent of their electric charge, only positively charged leptons are shown in the following calibration checks. Due to their low mass, the pseudorapidity approximation  $\eta$  is valid for the decay leptons. In each event, the lepton with the highest transverse momentum is referred to as the *leading lepton*, followed by *subleading leptons* with lower  $p_T$ . In this analysis, the leading lepton is labeled with index 1 and the first subleading lepton with index 2. Quantities involving contributions from both leptons carry the combined index 1,2.

#### Direction of the Leptons

Figure 13 illustrates the recoil component resolutions as a function of  $\phi$  and  $\eta$  as representative examples. The calibration of the hadronic recoil components with respect to the azimuthal angle  $\phi$  and the pseudorapidity  $\eta$  of the decay leptons shows good agreement between data and MC. Moreover, no significant dependence of the recoil components on either  $\phi$  or  $\eta$  is observed.



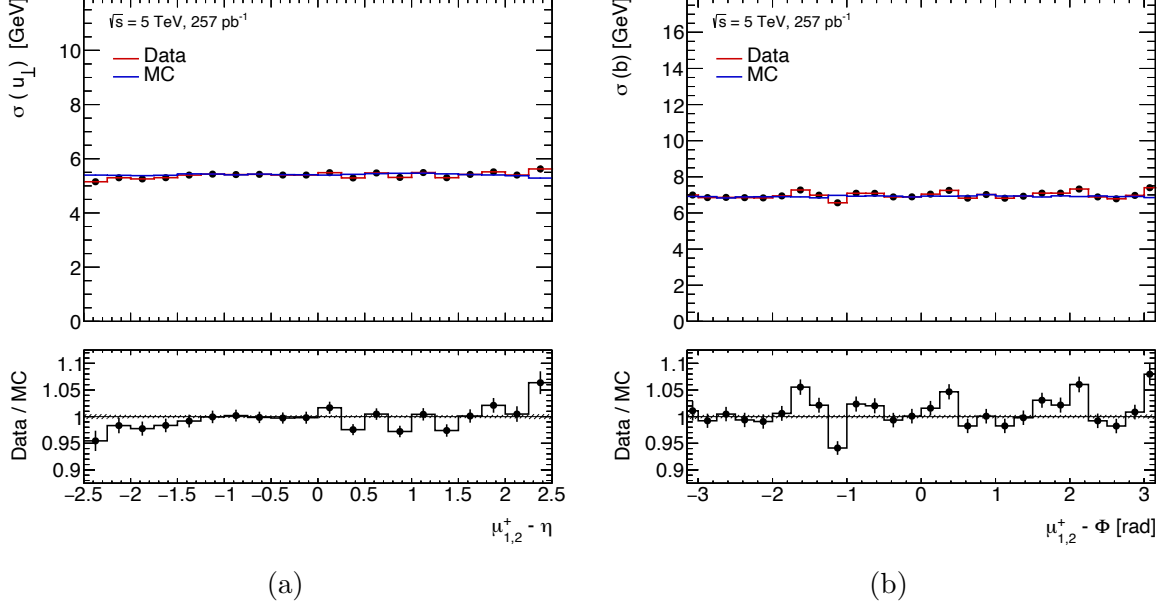


Figure 13: Data-to-MC comparison of (a) the resolution  $\sigma(u_{\perp})$  as a function of  $\eta$  and (b) the resolution  $\sigma(b)$  as a function of  $\phi$  for the positive leading and subleading leptons.

### Transverse Momentum of Leptons

The  $Z$  boson events used in this analysis are chosen based on distinct selection criteria. One of the requirements is that exactly two leptons with  $p_T^{\ell_{1,2}} > 25$  GeV are reconstructed.

Figure 14 shows that the MC simulation reproduces the data very well. A minimum of  $\langle b \rangle$ , and thus the best estimation of  $u_{\parallel}$ , is observed at  $p_T^{\ell_{1,2}} = 45$  GeV. The best resolution  $\sigma(b)$  is also achieved at this value. This can be explained by comparing the kinematic correlation between the  $Z$  boson transverse momentum  $p_T^Z$  and the transverse momenta of the leading  $p_T^{\ell_1}$  and subleading  $p_T^{\ell_2}$  leptons, as shown in Figure 15.

For  $p_T^Z \approx 0$  GeV, both the leading and subleading leptons have transverse momenta of about  $p_T^{\ell_{1,2}} = 45$  GeV. This case corresponds to the decay of a  $Z$  boson at rest in the transverse plane, where its rest energy of  $m_Z \approx 91$  GeV is equally distributed between the two leptons decaying fully transversely. Yet, a low  $p_T^Z$  implies little hadronic activity, resulting in simpler event reconstruction compared to events with significant hadronic recoil caused by higher  $p_T^Z$ .

As the  $Z$  boson's transverse momentum increases, the transverse momenta of the decay leptons adjust accordingly. The leading lepton may exceed  $p_T^{\ell_1} > 45$  GeV, while the subleading lepton may fall below  $p_T^{\ell_2} < 45$  GeV. Thus, events within  $p_T^{\ell_{1,2}} < 45$  GeV can be primarily associated with subleading leptons, while those within  $p_T^{\ell_{1,2}} > 45$  GeV are dominated by the leading lepton.

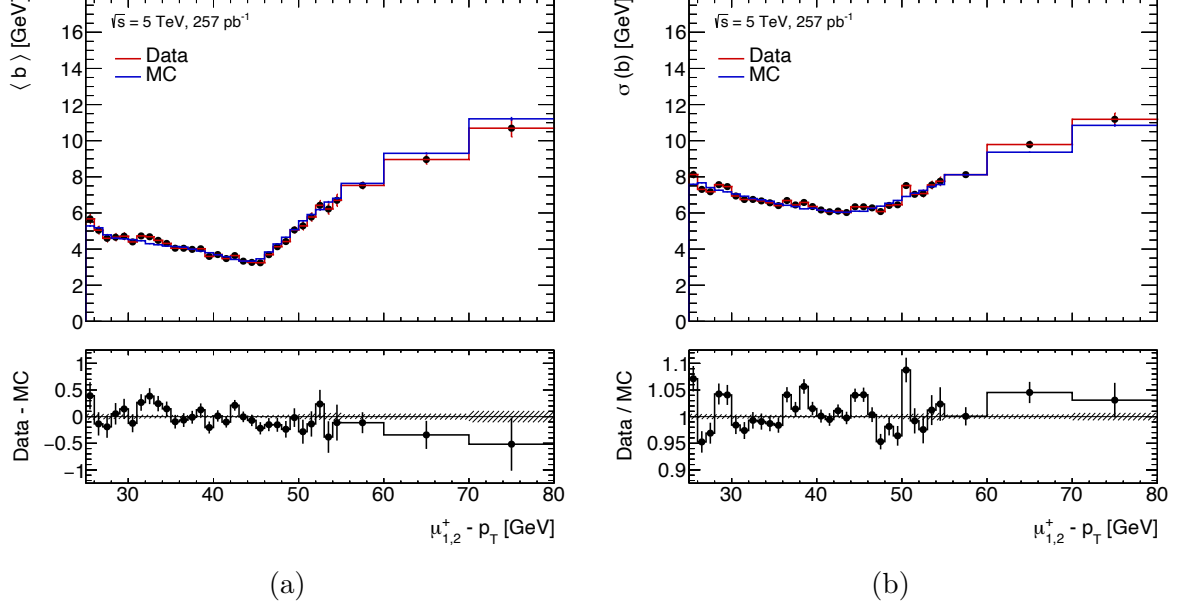


Figure 14: Data-to-MC comparison of (a) mean value  $\langle b \rangle$  and (b) the resolution  $\sigma(b)$  of the bias as a function of the transverse momentum  $p_T$  of the leading and subleading positive lepton  $\mu_{1,2}^+$ .

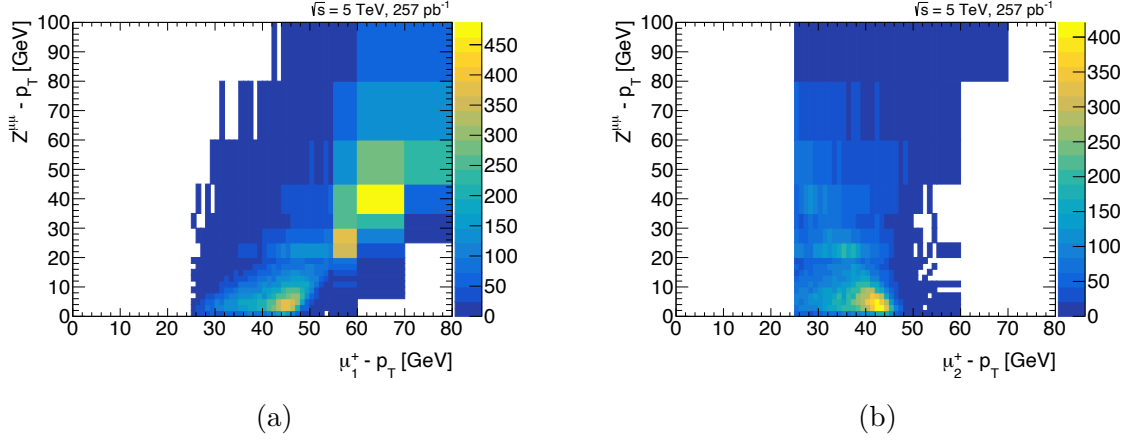


Figure 15: Two-dimensional Histograms of the  $Z$  boson transverse momentum  $p_T^Z$  as a function of the transverse momentum  $p_T$  of (a) the leading positive lepton  $\mu_1^+$  and (b) the subleading positive lepton  $\mu_2^+$ .

This becomes even clearer when comparing Figure 14b with Figure 16. In Figure 16a, which shows the  $\sigma(b)$  dependence on the leading lepton transverse momentum  $p_T^{\ell_1}$ , the resolution remains minimal and constant for  $p_T^{\ell_1} \leq 45$  GeV. In this range, the sum  $p_T^{\ell_1} + p_T^{\ell_2}$  is below 91 GeV, because the decay plane is tilted with respect to the transverse plane. As shown in Figure 15a,  $p_T^{\ell_1} \leq 45$  GeV occurs rarely and only for low  $p_T^Z$ , which explains the good resolution due to the reduced hadronic activity in these events. Furthermore, for  $p_T^{\ell_1} > 45$  GeV, most events coincide with a subleading lepton with  $p_T^{\ell_2} < 45$  GeV.

In this case, as illustrated in Figure 15, the  $Z$  boson has a higher  $p_T^Z$ , resulting in increased hadronic activity and consequently higher values of  $\langle b \rangle$  and  $\sigma(b)$ . This explains the similarities between the curves in Figure 16 and Figure 14b in the respective  $p_T^{\ell_{1,2}}$  range. Leading leptons are more likely to have  $p_T^{\ell_1} > 45$  GeV, while subleading leptons tend to have  $p_T^{\ell_2} < 45$  GeV. Due to this statistical imbalance, each lepton type dominates its respective transverse momentum region in Figure 14b. The high deviations for  $p_T^{\ell_2} > 45$  GeV in Figure 16b are due to limited statistics. Since for the subleading lepton  $p_T^{\ell_2} < p_T^{\ell_1}$  applies, such events require very high  $p_T^Z$  and are accompanied by significant hadronic activity.

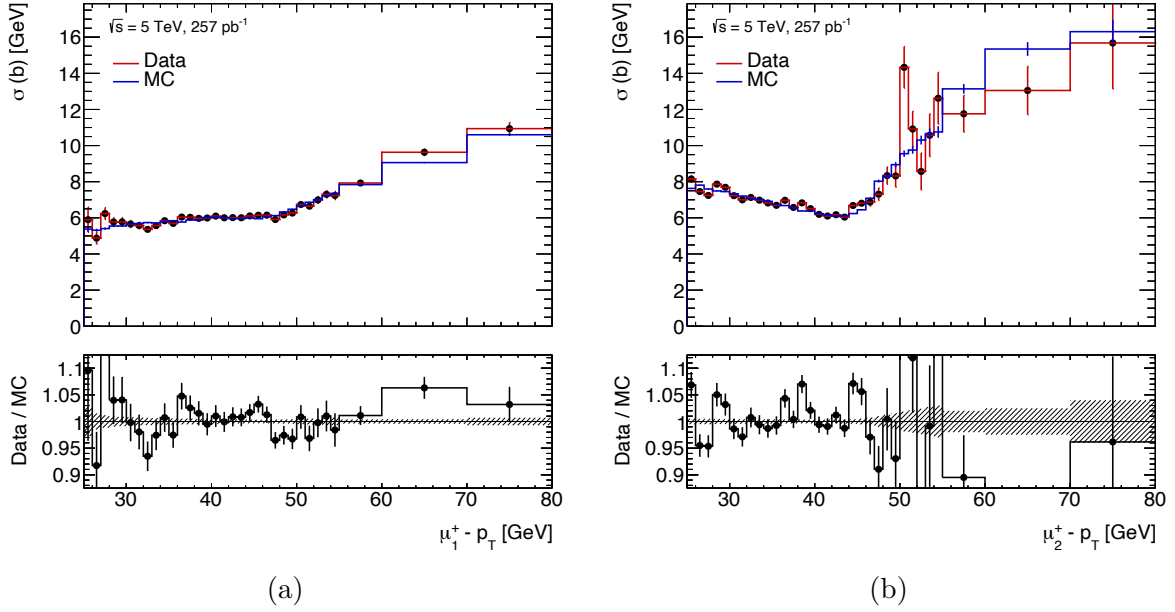


Figure 16: Data-to-MC comparison of the resolution  $\sigma(b)$  of the bias as a function of the transverse momentum  $p_T$  of (a) the leading positive lepton  $\mu_1^+$  and (b) the subleading positive lepton  $\mu_2^+$ .

Besides, an optional event selection requiring  $u_T < 25$  GeV can be applied. The impact of this selection on the calibration checks is discussed in Appendix B. Overall, applying this additional cut still yields good agreement between data and MC simulation.

## 6 Electron Charge Misidentification

In addition to the calibration of the hadronic recoil, other effects must be considered. One important aspect is the misidentification of a lepton’s electric charge, in which the reconstructed charge of a lepton is opposite to its true charge, known as a *charge flip*. Understanding the conditions under which charge flips occur is essential for correcting them in the simulation. Due to the production asymmetry between  $W^+$  and  $W^-$  bosons in pp collisions at the LHC, see Subsection 3.1, charge flip effects do not cancel out and can introduce a bias if not properly accounted for.

In order to calibrate the MC simulation for lepton charge misidentification,  $Z$  boson events are analyzed. The same event selection criteria as in the recoil calibration are applied, including the additional cut  $u_T < 25 \text{ GeV}$ , which is discussed in Appendix B. The only modification to the event selection is the requirement that both leptons have the same electric charge, i.e.  $Z \rightarrow \ell^\pm \ell^\pm$ . Physically, this violates charge conservation, as the  $Z$  boson is electrically neutral. However, incorrectly reconstructed decays may appear as such in the detector.

The analysis is performed with data at center-of-mass energies of 5 TeV and 13 TeV, corresponding to integrated luminosities of  $257 \text{ pb}^{-1}$  and  $335 \text{ pb}^{-1}$ , respectively. Using the integrated fiducial cross sections from [19], the production ratio of  $W^+$  and  $W^-$  bosons is  $\sigma_f(W^+)/\sigma_f(W^-) = 1.61 \pm 0.03$  at 5 TeV and  $\sigma_f(W^+)/\sigma_f(W^-) = 1.31 \pm 0.02$  at 13 TeV. This analysis is only performed for the electron channel, since the muon charge can be measured with high accuracy in the ATLAS muon spectrometer. The plots presented below correspond to data at 5 TeV. The respective plots for 13 TeV are provided in Appendix C.

### 6.1 Comparison of Same-Sign and Opposite-Sign Events

The first step in the charge flip analysis is a data-to-MC comparison of events that pass either the *opposite-sign* event selection, indicating correctly reconstructed charges, or the *same-sign* selection, where a charge flip has occurred. An example of the invariant mass distributions at 5 TeV for both selections is shown in Figure 17. While the MC simulation aligns well with the data for opposite-sign events, a disagreement can be seen for same-sign events. For a detailed comparison, a bin-wise event ratio is constructed by dividing the number of same-sign events  $N_{ss}$  by the number of opposite-sign events  $N_{os}$ . The resulting data-to-MC comparison of this ratio also shows significant deviations. A comparable disagreement can be noticed for the corresponding analysis at 13 TeV.

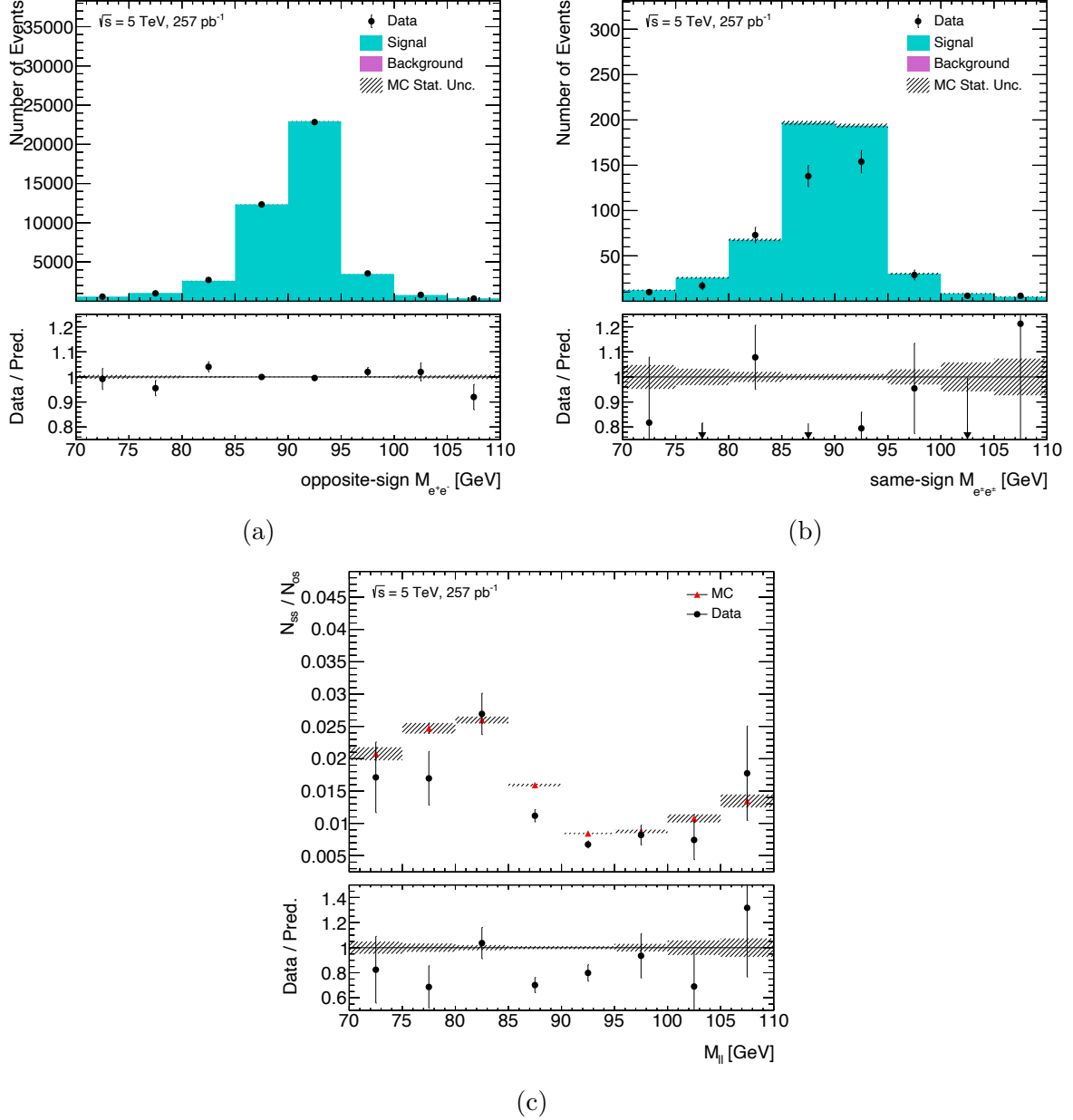


Figure 17: A data-to-MC comparison of the invariant mass distribution for (a) opposite-sign and (b) same-sign events. Accordingly, the bin-wise ratio of same-sign events  $N_{ss}$  divided by opposite-sign events  $N_{os}$  for data and MC can be seen in (c).

To gain a better understanding of the origin of charge misidentification, the  $|\eta|$  and  $p_T$  distributions of the leading and subleading leptons are analyzed following the same procedure as for the invariant mass distribution. A representation of this analysis is shown in Figure 18 for the leading lepton at 5 TeV. Similar behavior is observed for the subleading lepton, as well as for both leptons at 13 TeV.

The results show a systematic overestimation of the MC simulation signal in same-sign events. In particular, the ratio of same-sign to opposite-sign events for high  $|\eta|$  regions is larger than for low  $|\eta|$  regions. In contrast, the same ratio appears to be independent as

a function of  $p_T$ , despite the constant overestimation.

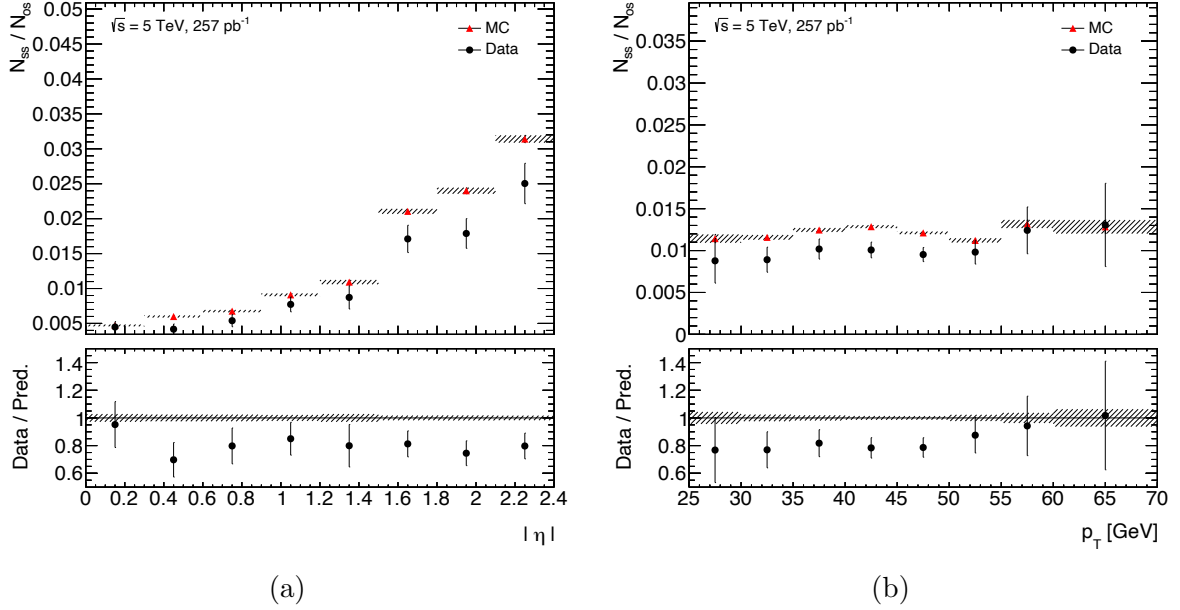


Figure 18: The bin-wise ratio of same-sign events  $N_{ss}$  divided by opposite-sign events  $N_{os}$  (a) as a function of  $|\eta|$  and (b) as function of  $p_T$  for the leading lepton at 5 TeV.

## 6.2 Single Electron Charge Identification

The comparison of opposite-sign and same-sign events imply that charge misidentification occurs at both 5 TeV and 13 TeV in regions with high  $|\eta|$ . This requires the derivation of a correction factor for the simulation. To achieve this, the single electron charge misidentification probability, denoted as  $\varepsilon^{\text{chgMisID}}$ , must be determined. The method used to obtain this probability is described in detail in [20]. A brief overview is given below. The derivation relies on the following assumptions:

- $\varepsilon^{\text{chgMisID}}$  is independent of the electron's true charge,
- $\varepsilon^{\text{chgMisID}}$  can be described as a function of reconstructed electron variables such as pseudorapidity  $\eta$  or transverse momentum  $p_T$ ,
- the charge misidentification of one decay electron does not correlate to the other in  $Z \rightarrow e^+e^-$ ,
- the probability that both electrons from the same decay are misidentified is negligible.

For the derivation of  $\varepsilon^{\text{chgMisID}}$ , the event number of same-sign electron pairs,  $N_{ij}^{\text{wrong}}$ , and the total event number of electron pairs,  $N_{ij}^{\text{all}}$ , are needed. The index  $i$  ( $j$ ) denotes the bin in which the leading electron  $e_1$  (or subleading electron  $e_2$ ) was reconstructed, respectively. Assuming for now that the misidentification probability depends only on  $|\eta|$ , then, for  $n$

bins with corresponding  $\varepsilon^{\text{chgMisID}}(|\eta_i|)$ , there exist  $n(n+1)/2$  equations of the type

$$N_{ij}^{\text{wrong}} = N_{ij}^{\text{all}} \left( \varepsilon^{\text{chgMisID}}(|\eta_i|) + \varepsilon^{\text{chgMisID}}(|\eta_j|) \right), \quad 1 \leq i, j \leq n. \quad (15)$$

An illustration of the distributions  $N_{ij}^{\text{wrong}}$  and  $N_{ij}^{\text{all}}$  binned in  $|\eta|$  for data at 5 TeV is shown in Figure 19, indicating a dependence of the charge misidentification probability on  $|\eta|$ .

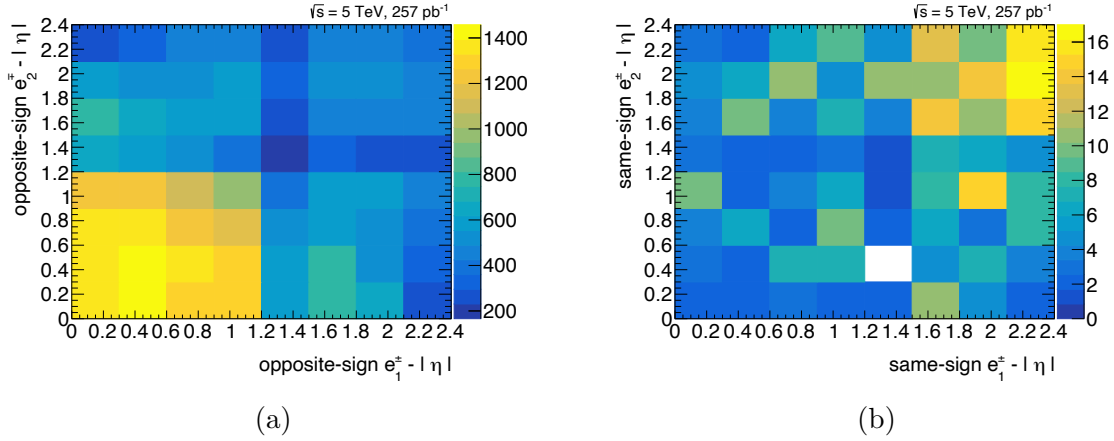


Figure 19: Correlation of absolute pseudorapidities  $|\eta|$  from leading electron  $e_1$  and sub-leading electron  $e_2$  requiring (a) opposite-sign pairs and (b) same-sign pairs with bins representing  $N_{ij}^{\text{wrong}}$ . Adding both histograms yields bins representing  $N_{ij}^{\text{all}}$ .

Next, a Maximum Likelihood Fit is performed to determine  $\varepsilon^{\text{chgMisID}}(|\eta_i|)$ . The Log Likelihood function is constructed by summing over all combinations of  $|\eta|$  bins  $(i, j)$ :

$$L = \sum_{(ij)} \log P \left( N_{ij}^{\text{wrong}}, N_{ij}^{\text{all}}, \varepsilon^{\text{chgMisID}}(|\eta_i|), \varepsilon^{\text{chgMisID}}(|\eta_j|) \right). \quad (16)$$

Here,  $P$  denotes the Poisson probability distribution based on two summed up Poisson-distributed parameters,  $\lambda_{ij} = N_{ij}^{\text{all}} \varepsilon^{\text{chgMisID}}(|\eta_i|)$  and  $\mu_{ij} = N_{ij}^{\text{all}} \varepsilon^{\text{chgMisID}}(|\eta_j|)$ , hence

$$\lambda_{ij} + \mu_{ij} = N_{ij}^{\text{all}} \left( \varepsilon^{\text{chgMisID}}(|\eta_i|) + \varepsilon^{\text{chgMisID}}(|\eta_j|) \right). \quad (17)$$

Therefore, the Poisson distribution is given by

$$P \left( N_{ij}^{\text{wrong}}, N_{ij}^{\text{all}}, \varepsilon^{\text{chgMisID}}(|\eta_i|), \varepsilon^{\text{chgMisID}}(|\eta_j|) \right) = \frac{(\lambda_{ij} + \mu_{ij})^{N_{ij}^{\text{wrong}}}}{N_{ij}^{\text{wrong}}!} e^{-(\lambda_{ij} + \mu_{ij})}. \quad (18)$$

The results of the Maximum Likelihood Fit yield the single electron charge misidentification probability  $\varepsilon^{\text{chgMisID}}$  as a function of  $|\eta|$  for both data and MC, as shown in

Figure 20a.<sup>2</sup> At low  $|\eta|$ , the MC simulation agrees well with the data points, indicating that the charge misidentification probability is well modeled in this region. However, at higher values of  $|\eta|$ , the MC significantly overestimates the probability, confirming that a correction factor for the simulation is needed.

A Maximum Log Likelihood Fit performed under the assumption that  $\varepsilon^{\text{chgMisID}}$  depends on  $p_T$  yields the results shown in Figure 20b. Although the MC simulation consistently overestimates the charge misidentification probability, no significant dependence on  $p_T$  is observed. A similar behavior in both  $\eta$  and  $p_T$  dependence is observed in the 13 TeV data. This indicates that the scale factor required to correct the MC simulation can indeed be treated as a function of  $|\eta|$  only. Applying this scale factor is expected to correct the overestimation of the MC prediction with respect to both  $|\eta|$  and  $p_T$ .

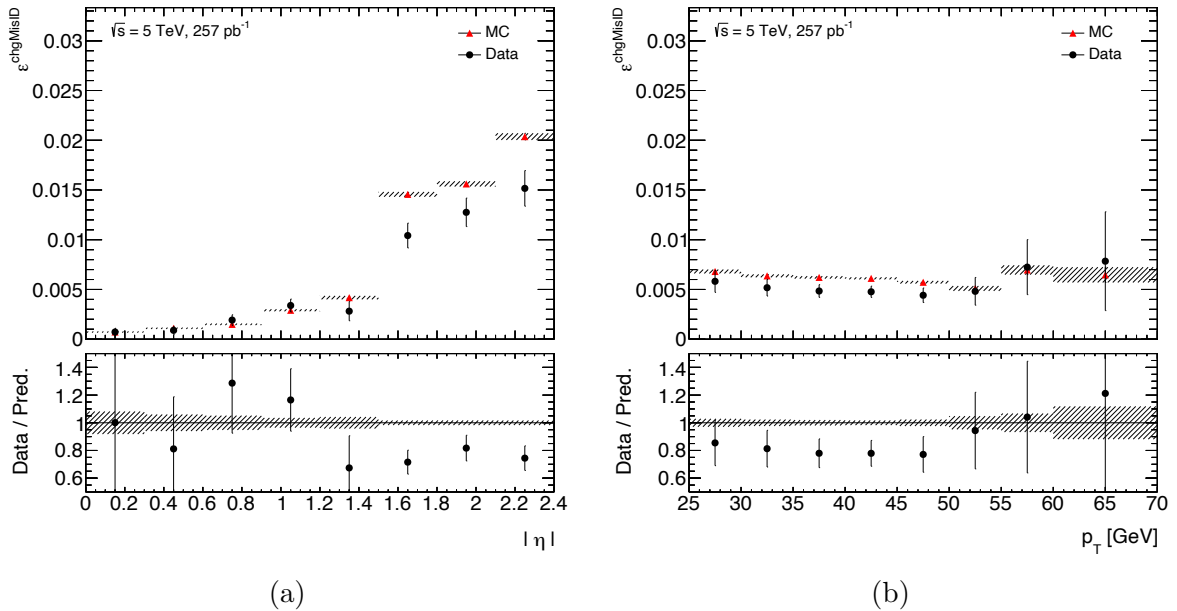


Figure 20: Results for the single electron charge misidentification probability  $\varepsilon^{\text{chgMisID}}$  for data and MC as a function of (a) the absolute pseudorapidity  $|\eta|$  and (b) the transverse momentum  $p_T$ , shown for data at 5 TeV.

Since  $\varepsilon^{\text{chgMisID}}(|\eta|)$  is now determined for both data,  $\varepsilon_{\text{data}}^{\text{chgMisID}}$ , and simulation,  $\varepsilon_{\text{MC}}^{\text{chgMisID}}$ , the scale factor correcting for charge misidentification in the MC can be computed separately for 5 TeV and 13 TeV as

$$f_{\text{wrong}}(|\eta|) = \frac{\varepsilon_{\text{data}}^{\text{chgMisID}}(|\eta|)}{\varepsilon_{\text{MC}}^{\text{chgMisID}}(|\eta|)}. \quad (19)$$

As both misidentification probabilities depend on  $|\eta|$ , the scale factor  $f_{\text{wrong}}$  is also a func-

<sup>2</sup>In principle,  $\varepsilon^{\text{chgMisID}}$  could be determined simultaneously as a function of both  $|\eta|$  and  $p_T$ . However, as Figure 19b indicates, the number of same-sign events is limited, making a multi-dimensional analysis of  $\varepsilon^{\text{chgMisID}}(|\eta|, p_T)$  statistically unreliable. Therefore, the  $\varepsilon^{\text{chgMisID}}$  is first evaluated as a function of only  $|\eta|$  and subsequently as a function of only  $p_T$ .



tion of  $|\eta|$  [21].

These derived scale factors can now be compared to the standard ATLAS Run 2 charge misidentification scale factors, which were obtained from long-duration, high pile-up runs and are therefore based on higher statistics, for details see [22, Section 9]. Figure 21a shows the comparison of scale factors as a function of  $|\eta|$ . The derived scale factors at low pile-up are integrated over all  $p_T$  values, while the standard scale factors from high pile-up events are provided in bins of  $p_T$ . In addition, Figure 21b compares the scale factors as a function of  $p_T$ , where the derived scale factors are integrated over  $|\eta|$  and the standard factors are given in separate  $|\eta|$  bins, excluding the tile gap region. Despite the different pile-up conditions, the derived and standard scale factors show an overall agreement within uncertainties.

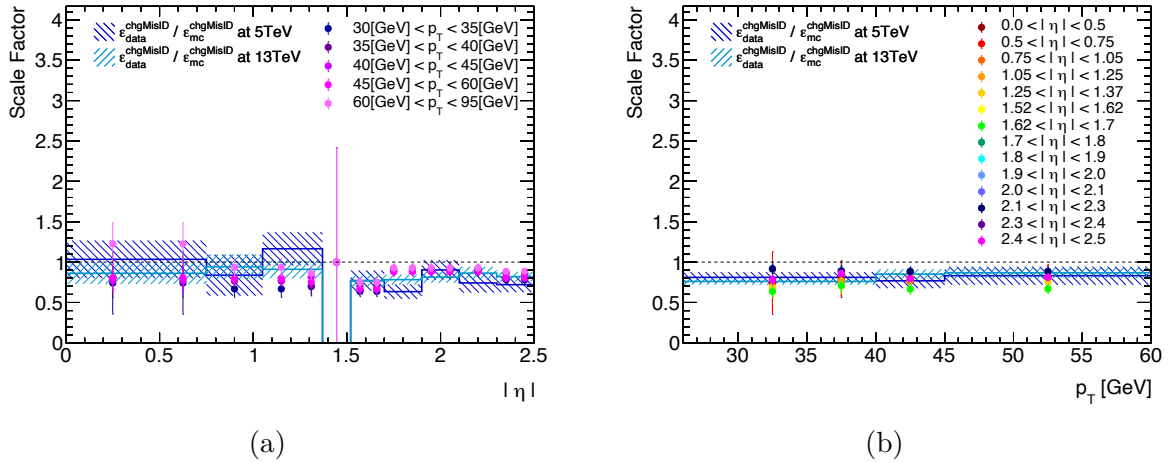


Figure 21: Comparison of derived scale factors at 5 TeV and 13 TeV with standard ATLAS scale factors (a) as a function of  $|\eta|$  and (b) as a function of  $p_T$ .

This observation implies that in this analysis, electron charge misidentification does not primarily occur due to reduced curvature at high lepton transverse momentum, but rather due to effects related to the detector geometry and construction. One major reason for the increased misidentification probability in high  $|\eta|$  regions is the limited coverage of the TRT, which only extends up to  $|\eta| < 2$ , thus restricting extended track reconstruction in the ID for larger pseudorapidities [23].

Furthermore, physics processes such as electron bremsstrahlung must be taken into account. Two possible scenarios are illustrated in Figure 22. In the first case, the emitted bremsstrahlung photon can produce an electron–positron pair and the track reconstruction algorithm might mistakenly associate the original electron track with that of the oppositely charged electron resulting from the photon conversion [21]. Similarly, if the electron resulting from the conversion carries the same charge as the original one but both escape detection due to  $|\eta| > 2.5$ , the reconstructed track may incorrectly correspond to

the oppositely charged electron.

Electron efficiencies in the ATLAS experiment during Run 2 have been studied in detail, confirming that the reconstruction performance decreases in the calorimeter transition region and at higher  $|\eta|$  values. For further details, see [23, Section 6].

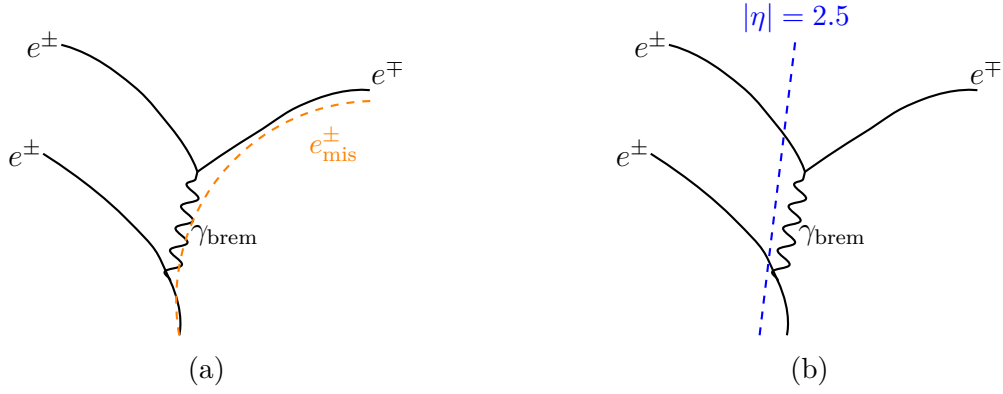


Figure 22: Two scenarios in which bremsstrahlung can lead to electron charge misidentification: (a) Incorrect association of the particles track after after bremsstrahlung or (b) initial electron escaping detection beyond  $|\eta| > 2.5$  while the bremsstrahlung electron with opposite charge is misidentified as the primary particle.

In summary, for this analysis, the simulation can be corrected using the standard scale factors for Run 2 provided by the ATLAS Collaboration. By applying these corrections, the analysis benefits from the larger statistics on which the standard scale factors are based.

## 7 Conclusion

A precise measurement of the  $W$  boson mass is a profound test of the Standard Model and may reveal signs of new physics. The ATLAS Collaboration contributes to this research using Run 2 data taken under low pile-up conditions and including multiple decay channels.

For an accurate mass determination, the hadronic recoil must be modeled precisely, which is achieved through a calibration based on  $Z \rightarrow \ell^+ \ell^-$  events, where the lepton kinematics are fully reconstructible. In this thesis, the calibration of the simulation was examined.

First, recoil calibration checks were performed as a function of both  $Z$  boson properties and lepton kinematics, focusing on aspects not explicitly covered in the standard calibration. No significant dependence of the hadronic recoil on the  $Z$  boson rapidity was observed, confirming the validity of the existing calibration procedure. A dependence on the  $Z$  boson transverse momentum was identified and the MC simulation accurately reproduced the measured distributions. In addition, the recoil response was studied with respect to the kinematics of the decay leptons. The recoil was found to be independent of the lepton decay direction. The calibration as a function of the lepton transverse momentum was also validated. A dependence related to the distinction between leading and subleading leptons was observed across different  $p_T^\ell$  regions, but this effect was well understood and consistent with expectations.

Besides recoil calibration, other effects affecting the  $W$  boson decay reconstruction have also been studied. One such effect is the charge misidentification of electrons and positrons, which is particularly relevant due to the asymmetric production of  $W^+$  and  $W^-$  bosons at the LHC.

An initial data-to-MC comparison, using  $Z \rightarrow e^\pm e^\pm$  events with same-sign lepton pairs, revealed significant discrepancies, requiring further investigation. Therefore, the charge misidentification probability was extracted as a function of  $|\eta|$  and  $p_T$  using a Maximum Likelihood Fit based on Poisson statistics. It was shown that the misidentification probability increases with the electron's absolute pseudorapidity, while no strong dependence on the transverse momentum was observed.

Finally, the correction scale factors derived from this analysis were compared to standard Run 2 ATLAS scale factors obtained from high pile-up data with greater statistical precision. The comparison showed good agreement as a function of both  $|\eta|$  and  $p_T$ . Based on this consistency, it was concluded that the standard ATLAS scale factors can be reliably applied to correct the simulation.

The studies presented in this thesis have either confirmed the validity of the current modeling or enabled the extraction of correction factors where discrepancies were identified. These contributions improve the accuracy of the analysis and represent an important step toward the final  $W$  boson mass measurement.

# Appendix

## A Validation of the Hadronic Recoil Calibration for the Electron Channel

The recoil calibration was also validated in the electron decay channel  $Z \rightarrow e^+e^-$  at 5 TeV with an integrated luminosity of  $257 \text{ pb}^{-1}$ . A selection of corresponding validation plots, analogous to those presented for muons in Section 5, is shown here for the electron decay channel.

### Calibration Checks on $Z$ Boson Quantities

#### Rapidity of the $Z$ Boson

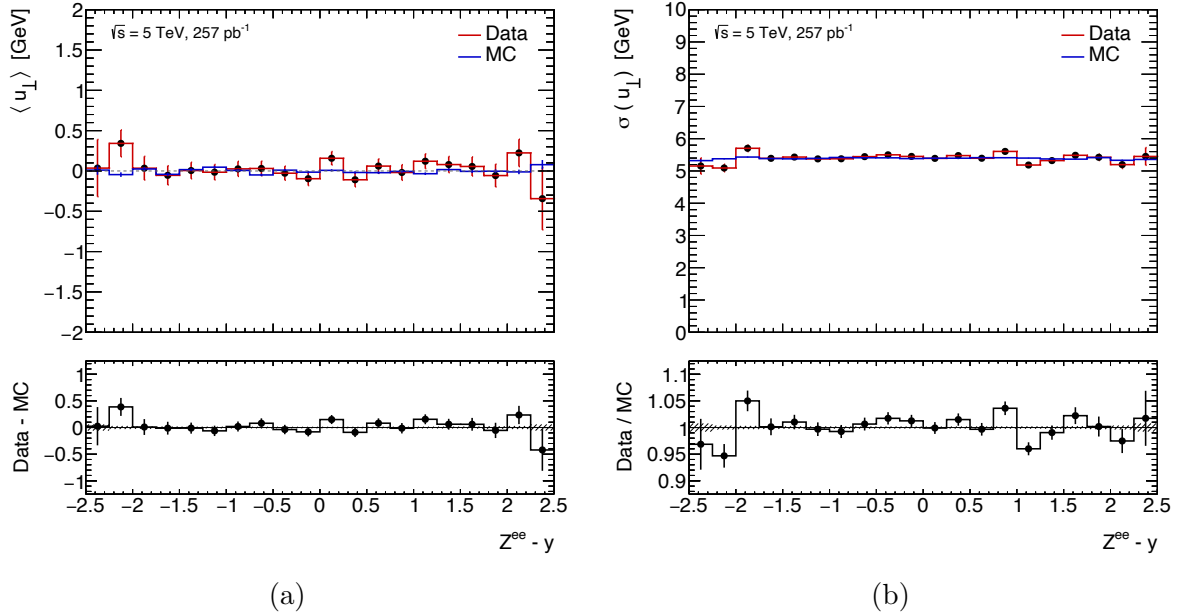


Figure 23: Data-to-MC comparison of (a) mean value  $\langle u_{\perp} \rangle$  and (b) resolution  $\sigma(u_{\perp})$  of the perpendicular hadronic recoil component as a function of the  $Z$  boson rapidity  $y$ .

## Transverse Momentum of the $Z$ Boson

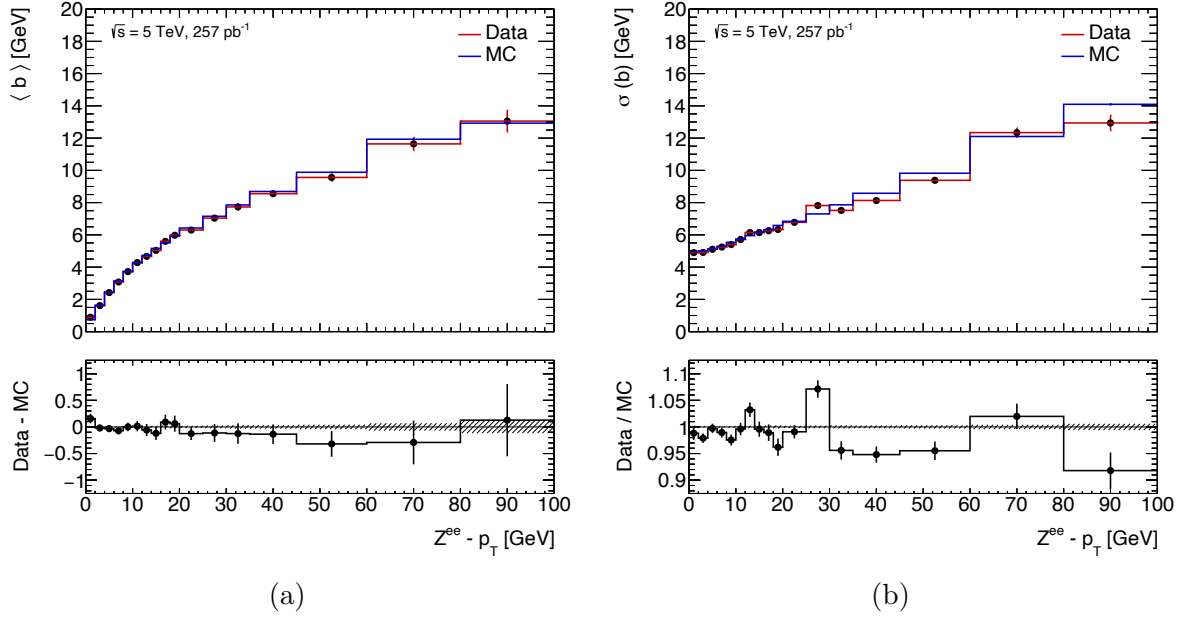


Figure 24: Data-to-MC comparison of (a) mean value  $\langle b \rangle$ , (b) absolute resolution  $\sigma(b)$  of the bias as a function of the  $Z$  boson transverse momentum  $p_T^Z$ .

## Calibration Checks on Lepton Quantities

### Direction of the Leptons

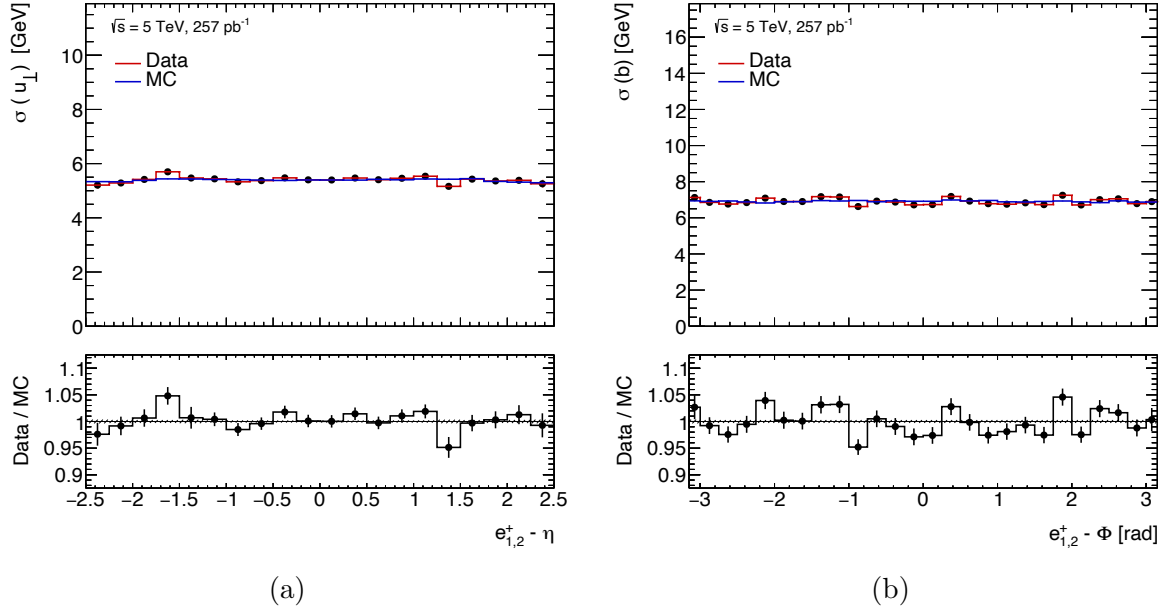


Figure 25: Data-to-MC comparison of (a) the resolution  $\sigma(u_{\perp})$  as a function of  $\eta$  and (b) the resolution  $\sigma(b)$  as a function of  $\phi$  for the positive leading and subleading leptons.

## Transverse Momentum of Leptons

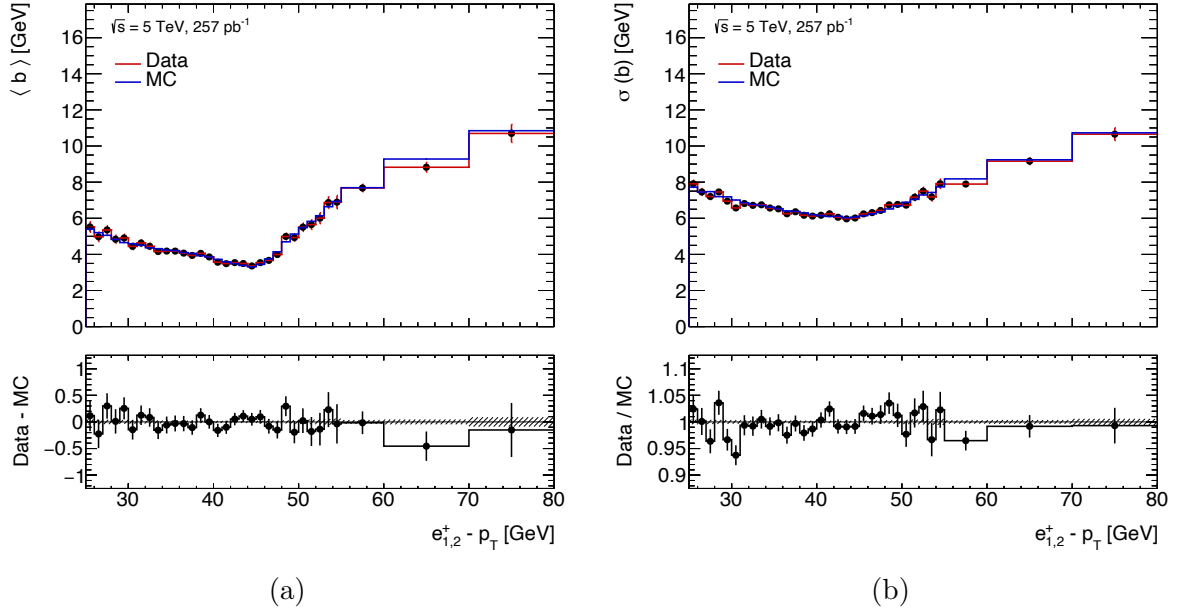


Figure 26: Data-to-MC comparison of (a) mean value  $\langle b \rangle$  and (b) the resolution  $\sigma(b)$  of the bias as a function of the transverse momentum  $p_T$  of the leading and subleading positive lepton  $e_{1,2}^+$ .

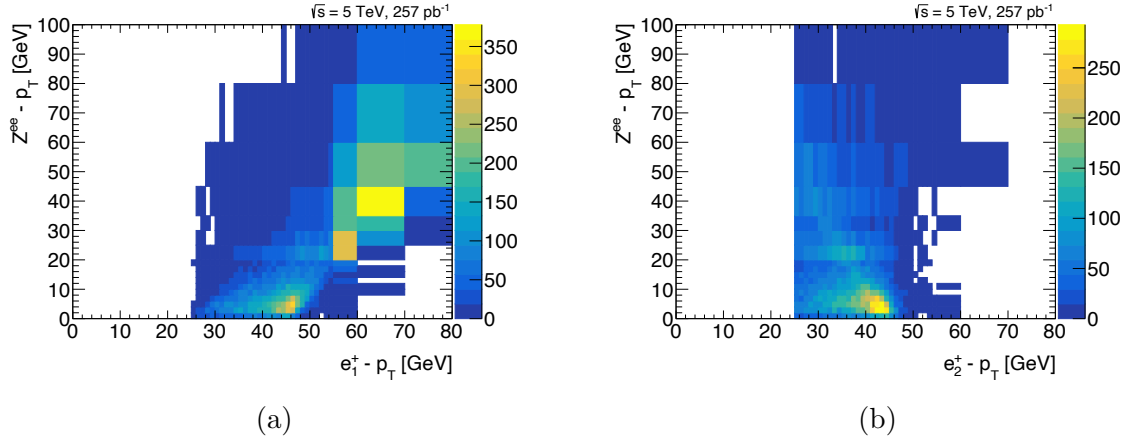


Figure 27: Two-dimensional Histograms of the  $Z$  boson transverse momentum  $p_T^Z$  as a function of the transverse momentum  $p_T$  of (a) the leading positive lepton  $e_1^+$  and (b) the subleading positive lepton  $e_2^+$ .

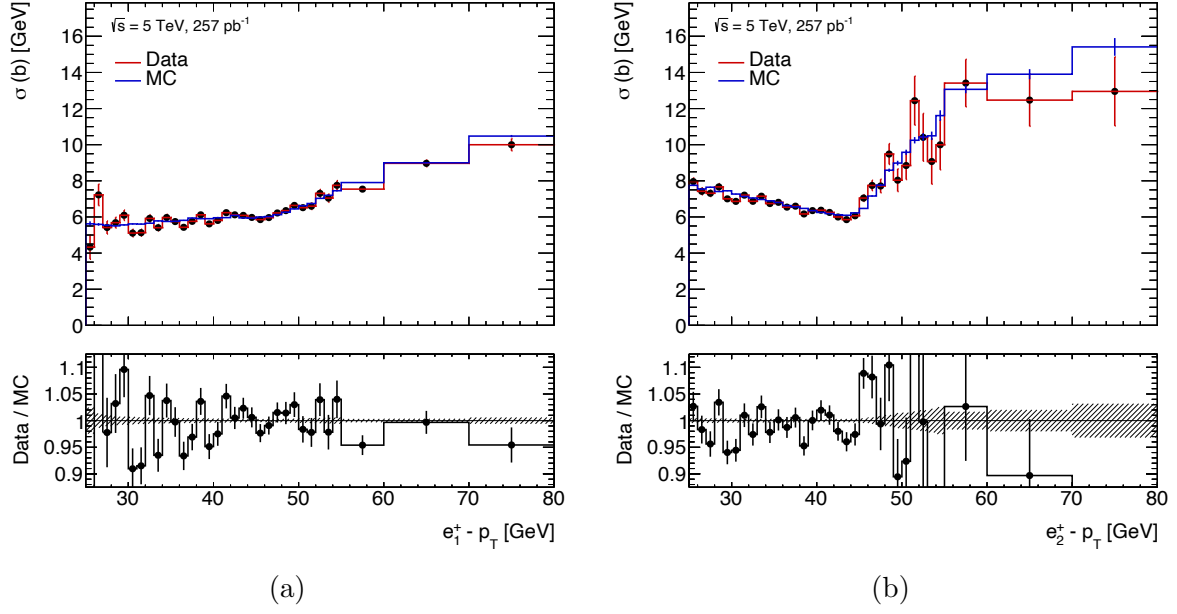


Figure 28: Data-to-MC comparison of the resolution  $\sigma(b)$  of the bias as a function of the transverse momentum  $p_T$  of (a) the leading positive lepton  $e_1^+$  and (b) the subleading positive lepton  $e_2^+$ .

## B Validation of the Hadronic Recoil Calibration with an Additional Selection Cut

Additionally, applying  $u_T < 25$  GeV as an event selection criterion mainly reduces hadronic activities. This improves both the estimation and resolution of the recoil components, since  $u_T$  is directly related to the transverse momentum of the  $Z$  boson,  $p_T^Z$ .

Measured events with  $p_T^Z > 25$  GeV despite the  $u_T < 25$  GeV requirement can be explained by particles of ISR escaping detection due to an insufficient  $4\pi$  coverage of the detector or from asymmetries in the underlying event that reduce the observed recoil.

As an example, the same calibration checks shown in Figure 11 for the muon decay channel  $Z \rightarrow \mu^+\mu^-$  at 5 TeV were repeated with this additional cut applied. The corresponding results can be seen in Figure 29.

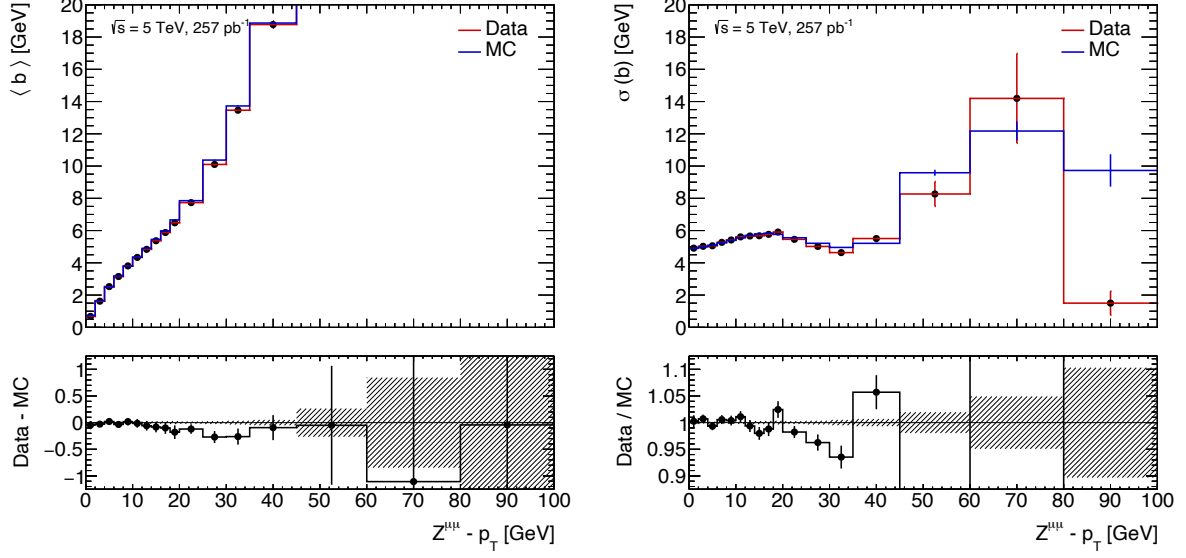
Analyzing the dependence of the mean bias  $\langle b \rangle$  on  $p_T^Z$ , it can be observed that for  $p_T^Z < 25$  GeV, the mean remains similar to the case without the  $u_T$  requirement. This indicates a good estimation of  $u_{\parallel}$ . However, for  $p_T^Z > 25$  GeV,  $\langle b \rangle$  increases rapidly. This is due to the fact, that requiring  $u_T < 25$  GeV cuts the Gaussian-like distribution of  $b$  in the lower tail, thereby shifting the mean  $\langle b \rangle$  toward higher values. The relation between  $u_T$  and  $b$  can be inferred from the following equations

$$|u_{\parallel}| < |u_T| = \sqrt{u_{\perp}^2 + u_{\parallel}^2} < 25 \text{ GeV} \quad \Rightarrow \quad |u_{\parallel}| = |b - p_T^Z| < 25 \text{ GeV} . \quad (20)$$

For a given value of  $p_T^Z$ , applying the  $u_T < 25$  GeV cut restricts the possible values of the bias  $b$  to a limited range. A demonstration of the cut performed on the  $b$  distribution leading to an increasing shift of  $\langle b \rangle$  can be seen in Figure 30 for the bin  $30 \text{ GeV} \leq p_T^Z \leq 35 \text{ GeV}$ .

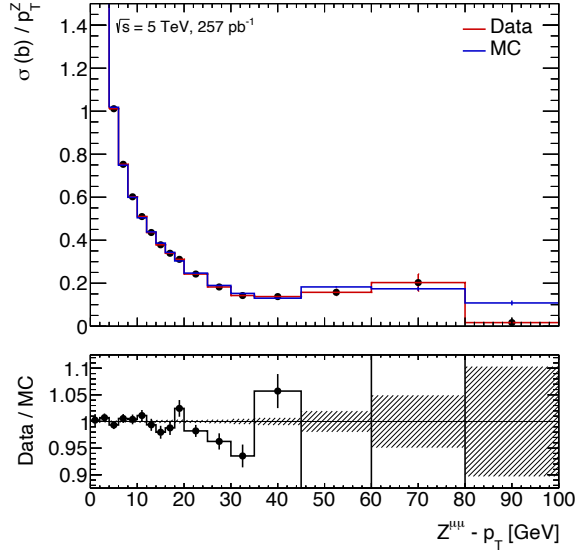
In addition, the calibration checks of  $\sigma(b)$  and the relative resolution  $\sigma(b)/p_T^Z$  indicate an improved bias resolution for  $p_T^Z < 25$  GeV due to reduced hadronic activity in the detector.





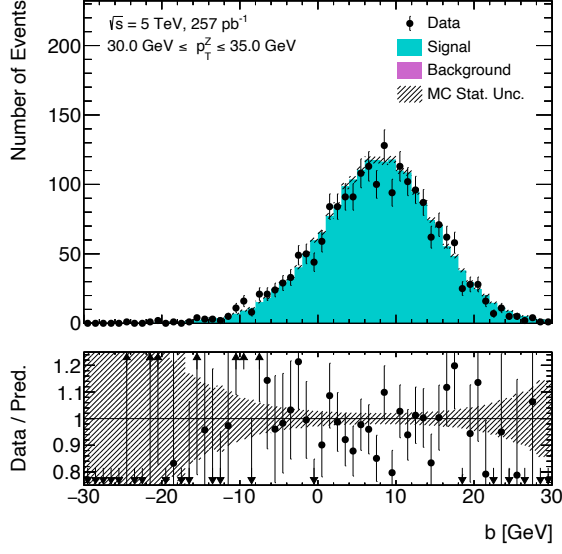
(a)

(b)

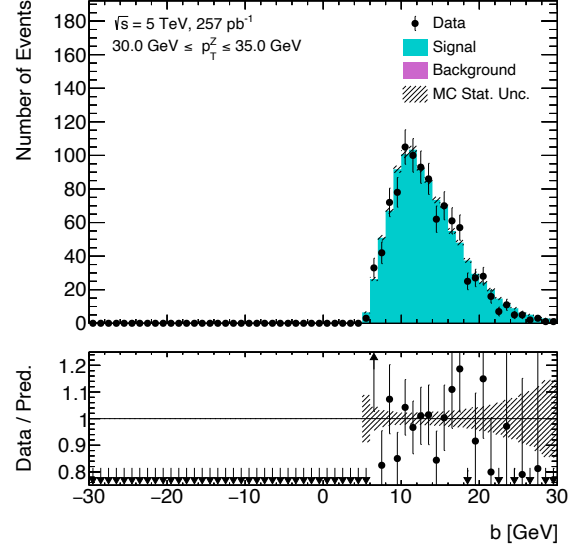


(c)

Figure 29: Data-to-MC comparison with additional  $u_T < 25$  GeV cut of (a) mean value  $\langle b \rangle$ , (b) absolute resolution  $\sigma(b)$  and (c) relative resolution  $\sigma(b)/p_T^Z$  of the bias as a function of the  $Z$  boson transverse momentum  $p_T^Z$ .



(a)



(b)

Figure 30: Data-to-MC comparison for the distribution of  $b$  in the bin  $30 \text{ GeV} \leq p_T^Z \leq 35 \text{ GeV}$  (a) without and (b) with event cut  $u_T < 25 \text{ GeV}$ .

## C Electron Charge Misidentification at 13 TeV

The analysis of electron charge misidentification was simultaneously performed for data at 13 TeV with an integrated luminosity of  $335, \text{pb}^{-1}$ . The corresponding validation plots, analogous to those presented for 5 TeV in Section 6, are shown here for 13 TeV.

### Comparison of Same-Sign and Opposite-Sign Events

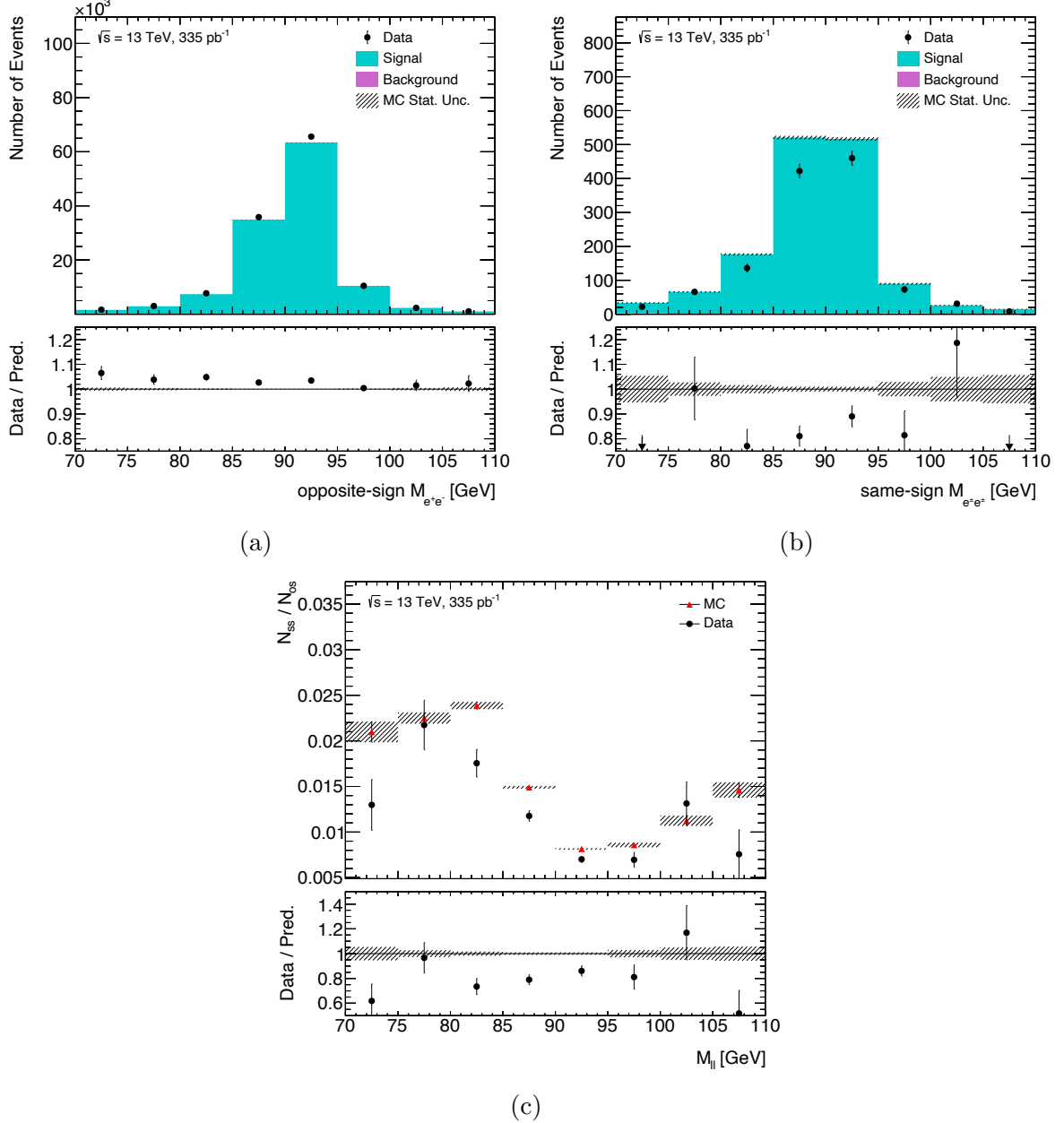


Figure 31: A data-to-MC comparison of the invariant mass distribution for (a) opposite-sign and (b) same-sign events. Accordingly, the bin-wise ratio of same-sign events  $N_{ss}$  divided by opposite-sign events  $N_{os}$  for data and MC can be seen in (c).

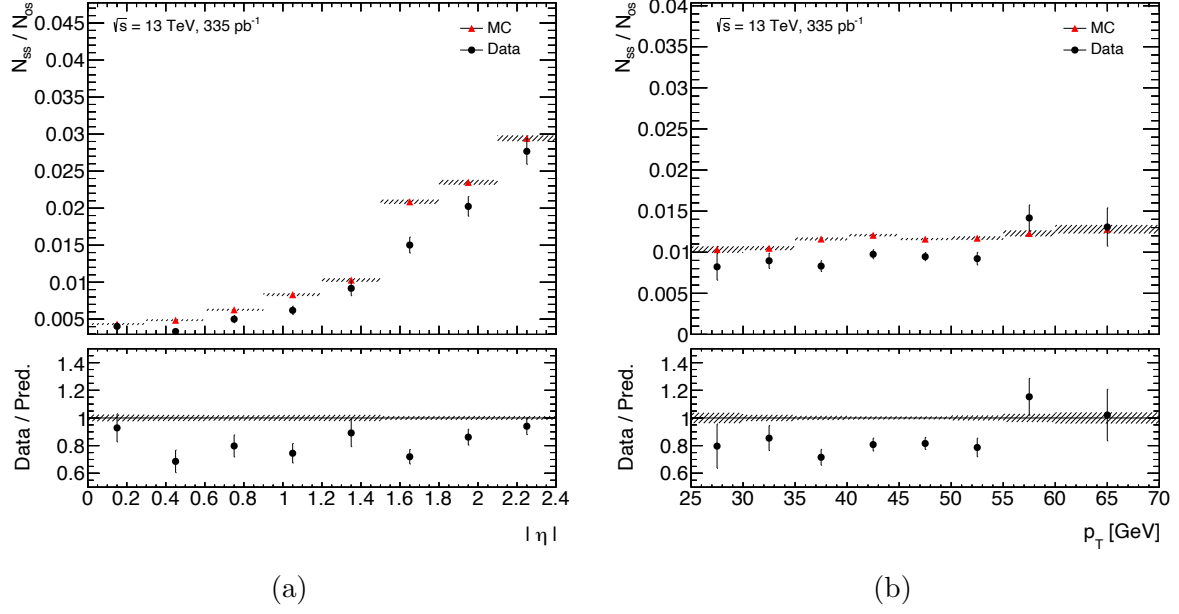


Figure 32: The bin-wise ratio of same-sign events  $N_{ss}$  divided by opposite-sign events  $N_{os}$  (a) as a function of  $|\eta|$  and (b) as function of  $p_T$  for the leading lepton at 13 TeV.

## Single Electron Charge Identification

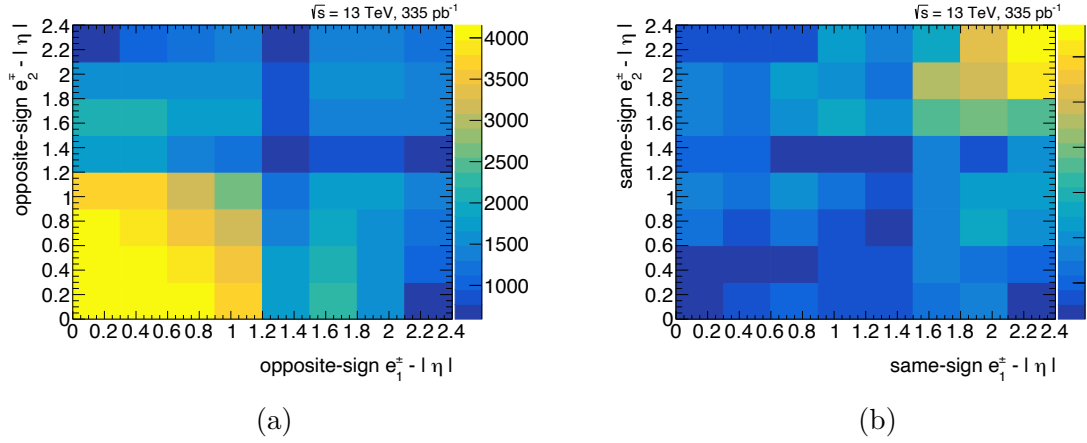


Figure 33: Correlation of absolute pseudorapidities  $|\eta|$  from leading electron  $e_1$  and sub-leading electron  $e_2$  requiring (a) opposite-sign pairs and (b) same-sign pairs with bins representing  $N_{ij}^{wrong}$ . Adding both histograms yields bins representing  $N_{ij}^{all}$ .

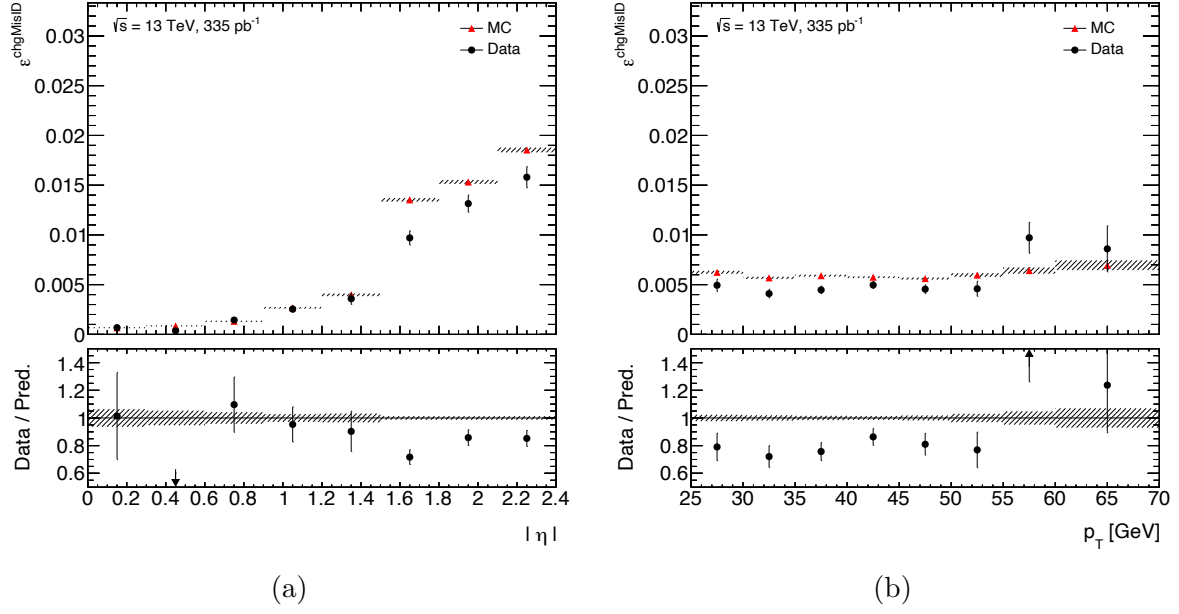


Figure 34: Results for the single electron charge misidentification probability  $\varepsilon^{\text{chgMisID}}$  for data and MC as a function of (a) the absolute pseudorapidity  $|\eta|$  and (b) the transverse momentum  $p_T$ , shown for data at 13 TeV.

## List of Abbreviations

<b>BSM</b>	Physics beyond the Standard Model
<b>CERN</b>	European Organization for Nuclear Research
<b>CMS</b>	Compact Muon Solenoid
<b>ID</b>	Inner Detector
<b>ISR</b>	Initial-state radiation
<b>LAr</b>	Liquid argon
<b>LEP</b>	Large Electron–Positron Collider
<b>LHC</b>	Large Hadron Collider
<b>MC</b>	Monte Carlo
<b>PDF</b>	Parton Distribution Function
<b>PFO</b>	Particle Flow Object
<b>pp</b>	Proton-proton
<b>SM</b>	Standard Model of particle physics
<b>TRT</b>	Transition Radiation Tracker

## Bibliography

- [1] The ATLAS Collaboration. “Measurement of the W-boson mass in pp collisions at  $\sqrt{s}=7\text{TeV}$  with the ATLAS detector”. In: *The European Physical Journal C* 78.110 (Feb. 2018). ISSN: 1434-6052. DOI: 10.1140/epjc/s10052-017-5475-4.
- [2] The CMS Collaboration. *High-precision measurement of the W boson mass with the CMS experiment at the LHC*. Dec. 2024. arXiv: 2412.13872.
- [3] The ATLAS Collaboration. *Hadronic recoil reconstruction and calibration for low pile-up runs taken in 2017 and 2018*. ATLAS Supporting Note ANA-STDM-2018-17-INT5. Geneva: CERN, Jan. 2023.
- [4] CERN. *The Large Hadron Collider*. URL: <https://home.web.cern.ch/science/accelerators/large-hadron-collider>. (visited on 16/07/2025).
- [5] The ATLAS Collaboration. *Measurement of the  $p_T$  spectrum of W and Z bosons produced in pp collisions at  $\sqrt{s} = 5\text{TeV}$  and 13 TeV in low-pileup runs*. ATLAS Internal Note ANA-STDM-2018-17-INT1. Geneva: CERN, Apr. 2023.
- [6] The ATLAS Collaboration. “The ATLAS Experiment at the CERN Large Hadron Collider”. In: *Journal of Instrumentation* 3.08 (Aug. 2008). ISSN: 1748-0221. DOI: 10.1088/1748-0221/3/08/S08003.
- [7] The ATLAS Experiment at CERN. *Detector & Technology*. URL: <https://atlas.cern/Discover/Detector>. (visited on 16/07/2025).
- [8] M. Aharrouche et al. “Study of the response of ATLAS electromagnetic liquid argon calorimeters to muons”. In: *Nuclear Instruments and Methods in Physics Research Section A: Accelerators, Spectrometers, Detectors and Associated Equipment* 606.3 (Aug. 2009). ISSN: 0168-9002. DOI: 10.1016/j.nima.2009.05.021.
- [9] The ATLAS Collaboration. *Operation of the ATLAS Trigger System in Run 2*. Oct. 2020. arXiv: 2007.12539.
- [10] M. Thomson. *Modern Particle Physics*. Cambridge, United Kingdom; New York: Cambridge University Press, 2013. ISBN: 978-1-107-03426-6.
- [11] The UA1 Collaboration. “Experimental observation of isolated large transverse energy electrons with associated missing energy at  $\sqrt{s} = 540\text{GeV}$ ”. In: *Phys. Lett. B* 122.1 (Feb. 1983). ISSN: 0370-2693. DOI: 10.1016/0370-2693(83)91177-2.
- [12] The UA1 Collaboration. “Experimental Observation of Lepton Pairs of Invariant Mass Around  $95\text{GeV}/c^2$  at the CERN SPS Collider”. In: *Phys. Lett. B* 126.5 (July 1983). ISSN: 0370-2693. DOI: 10.1016/0370-2693(83)90188-0.
- [13] The ATLAS Collaboration. *Observation of a new particle in the search for the Standard Model Higgs boson with the ATLAS detector at the LHC*. July 2012. arXiv: 1207.7214.
- [14] The CMS Collaboration. *Observation of a new boson at a mass of 125 GeV with the CMS experiment at the LHC*. July 2012. arXiv: 1207.7235.

- [15] S. Navas et al. (Particle Data Group). “54. Mass and Width of the W Boson”. In: *Phys. Rev. D* 110.03001 (May 2024). URL: <https://pdg.lbl.gov/2024/reviews/rpp2024-rev-w-mass.pdf>.
- [16] The ATLAS Collaboration. *Hadronic recoil reconstruction and calibration for low pile-up runs taken in 2017 and 2018*. ATLAS Supporting Note ANA-STDM-2018-17-INT5. (remade version by Oliver But). Geneva: CERN, Jan. 2023.
- [17] T. Dorigo. *Untitled*. 2000. URL: [https://www.science20.com/tommaso\\_dorigo/is\\_the\\_cdf\\_w\\_mass\\_measurement\\_a\\_nail\\_in\\_the\\_sm\\_coffin-256017](https://www.science20.com/tommaso_dorigo/is_the_cdf_w_mass_measurement_a_nail_in_the_sm_coffin-256017). (visited on 16/07/2025).
- [18] The ATLAS Collaboration. *Measurement of the W-boson mass and width with the ATLAS detector using proton-proton collisions at  $\sqrt{s} = 7\text{ TeV}$* . ATLAS Paper STDM-2019-24. Geneva: CERN, Mar. 2024.
- [19] The ATLAS Collaboration. *Precise measurements of W- and Z-boson transverse momentum spectra with the ATLAS detector using pp collisions at  $\sqrt{s} = 5.02\text{ TeV}$  and  $13\text{ TeV}$* . Nov. 2024. arXiv: 2404.06204.
- [20] The ATLAS Collaboration. *Double differential Z, W cross sections and their ratios in the electron channels*. ATLAS Internal Note ATL-PHYS-INT-2011-081. Geneva: CERN, Oct. 2011.
- [21] F. Illtzsche. “Observation of Electroweak Same-Charge  $W^{\pm}W^{\pm}jj$  Production at  $\sqrt{s} = 13\text{ TeV}$  with the ATLAS Detector at the LHC”. PhD thesis. Dresden University of Technology, 2019. URL: <https://repository.cern/records/fv00r-9ge60>.
- [22] The ATLAS Collaboration. *Electron and photon performance measurements with the ATLAS detector using the 2015-2017 LHC proton-proton collision data*. Dec. 2019. arXiv: 1908.00005.
- [23] The ATLAS Collaboration. *Electron and photon efficiencies in LHC Run 2 with the ATLAS experiment*. Nov. 2024. arXiv: 2308.13362.



## Acknowledgements

First and foremost, I would like to express my sincere thanks to Monica Dunford for giving me the opportunity to join her amazing research team. Being a part of the ATLAS group in Heidelberg has been a great pleasure and the chance to contribute to such a large collaboration has truly inspired and motivated me. Furthermore, I thank apl. Prof. Klaus Reygers for kindly agreeing to serve as the second examiner of this thesis.

Special thanks go to Jan Kretzschmar for providing the code used to determine the charge misidentification probability, as well as for valuable discussions and input, together with Raimund Ströhmer, Maarten Boonekamp, Ludovica Aperio Bella and Fabrice Balli.

I would like to express my deepest gratitude to Mathias, who guided me with patience every day throughout this journey. His profound explanations and thoughtful discussions motivated me, while his encouragement helped me to embrace new challenges. I am also thankful for his thorough proofreading of this thesis.

Thanks are also due to Anke, Thomas, Isa, Lisa and Varsiha for welcoming me into their group and for proofreading sections of my thesis.


I am extremely grateful to my best friends Paddy, Markus and Johanna, whom I have known since the first semester, when writing a bachelor's thesis in physics seemed like an insurmountable challenge. Spending what was probably every day of my studies with you was a joy and made everything feel easier.

Finally, I would like to thank my family for their unconditional support and belief in me.

# Erklärung

Ich versichere, dass ich diese Arbeit selbstständig verfasst und keine anderen als die angegebenen Quellen und Hilfsmittel benutzt habe.

Heidelberg, den 16.07.2025



---